Article

Humoral determinants of checkpoint immunotherapy

https://doi.org/10.1038/s41586-025-09188-4

Received: 23 February 2024

Accepted: 22 May 2025

Published online: 23 July 2025

Check for updates

Yile Dai[1,8], Lilach Aizenbud[2,8], Kai Qin[3,8], Matthew Austin[2], Jillian R. Jaycox[1], Joseph Cunningham[4], Eric Y. Wang[1], Lin Zhang[2], Suzanne Fischer[1], Sean M. Carroll[5], Helen van Aggelen[5], Yuval Kluger[4,6], Kevan C. Herold[1,7], Leon Furchtgott[5]✉, Harriet M. Kluger[2]✉ & Aaron M. Ring[3]✉

Although the role of cellular immunity in checkpoint immunotherapy (CPI) for cancer is well established[1,2], the effect of antibody-mediated humoral immunity is comparably underexplored. Here we used rapid extracellular antigen profiling[3] to map the autoantibody reactome within a cohort of 374 patients with cancer treated with CPIs and 131 healthy control participants for autoantibodies to 6,172 extracellular and secreted proteins (the 'exoproteome'). Globally, patients with cancer treated with CPIs had diverse autoreactivities that were elevated relative to control individuals but changed minimally with treatment. Autoantibody signatures in patients treated with CPI strikingly distinguished them from healthy individuals. Although associations of specific autoantibodies with immune-related adverse events were sparse, we detected numerous individual autoantibodies that were associated with greatly altered odds ratios for response to therapy. These included autoantibodies to immunomodulatory proteins, such as cytokines, growth factors and immunoreceptors, as well as tumour surface proteins. Functional evaluation of several autoantibody responses indicated that they neutralized the activity of their target proteins, which included type I interferons (IFN-I), IL-6, OSM, TL1A, and BMPR1A and BMPR2. Modelling the effects of autoantibodies to IFN-I and TL1A in preclinical mouse tumour models resulted in enhanced CPI efficacy, consistent with their effects in patients. In conclusion, these findings indicate that autoantibodies to the exoproteome modify CPI responses and highlight therapeutically actionable pathways that can be exploited to augment immunotherapy.

Although CPIs that target PD1, its ligand PDL1 and CTLA4 have been in clinical use for over a decade, it is unclear why these drugs exhibit extraordinary heterogeneity in outcomes[1,2,4]. Understanding the underlying factors that determine therapeutic responses is essential to extend the benefits of immunotherapy to more patients. Although most research on CPIs has been directed towards their effect on tumour-reactive T cells[2,5], emerging evidence has highlighted a potential role for B cells that mediate humoral (antibody-mediated) immunity[6,7]. The presence of tumour-infiltrating B cells and B cell-containing tertiary lymphoid structures in the tumour microenvironment is strongly associated with positive CPI treatment outcomes across multiple cancer types[8–10]. B cells have pleiotropic functions that include antigen presentation to T cells[11–13] as well as antibody production that may contribute to antitumour immunity. With respect to the latter function, autoantibodies (AAbs) that recognize tumour antigens such as HER2 and MUC1 are associated with enhanced survival[14,15]. However, few studies have comprehensively explored the breadth of AAb reactivities at a proteome scale (the 'AAb reactome') in patients with cancer.

Beyond their classical role in driving autoimmunity[16], self-reactive AAbs have been established to exert profound biological influences on health and disease. Notable examples include the devastating effects of anti-IFN-I AAbs in COVID-19 (refs. 17,18) and the protective effects of anti-amyloid-β AAbs in Alzheimer's disease[19]. With their ability to modulate the biological activity of their antigen targets, AAbs can thus contribute to an axis of phenotypic variation within the population that parallels the effects of genetics[20]. In this context, the exoproteome represents an important class of self-antigens targeted by AAbs. Antibodies are themselves large, secreted proteins that primarily exist in the extracellular compartment[21]. Consequently, the most readily accessible targets to AAbs are those that reside in the extracellular space. To detect the presence of potentially functional AAbs, we previously developed a high-throughput method, rapid extracellular antigen profiling (REAP), which is capable of detecting AAbs to several thousand human extracellular and secreted proteins simultaneously[3].

Here we hypothesized that patients with cancer have a range of AAbs that exert treatment-enhancing or treatment-inhibiting effects on CPIs. Identification of such antibody responses could help to explain

[1]Department of Immunobiology, Yale School of Medicine, New Haven, CT, USA. [2]Yale Cancer Center, New Haven, CT, USA. [3]Division of Translational Science and Therapeutics, Fred Hutchinson Cancer Center, Seattle, WA, USA. [4]Program of Applied Mathematics, Yale University, New Haven, CT, USA. [5]Seranova Bio, South San Francisco, CA, USA. [6]Department of Pathology, Yale University School of Medicine, New Haven, CT, USA. [7]Department of Internal Medicine, Yale School of Medicine, New Haven, CT, USA. [8]These authors contributed equally: Yile Dai, Lilach Aizenbud, Kai Qin. ✉e-mail: leon@seranovabio.com; harriet.kluger@yale.edu; aaronring@fredhutch.org

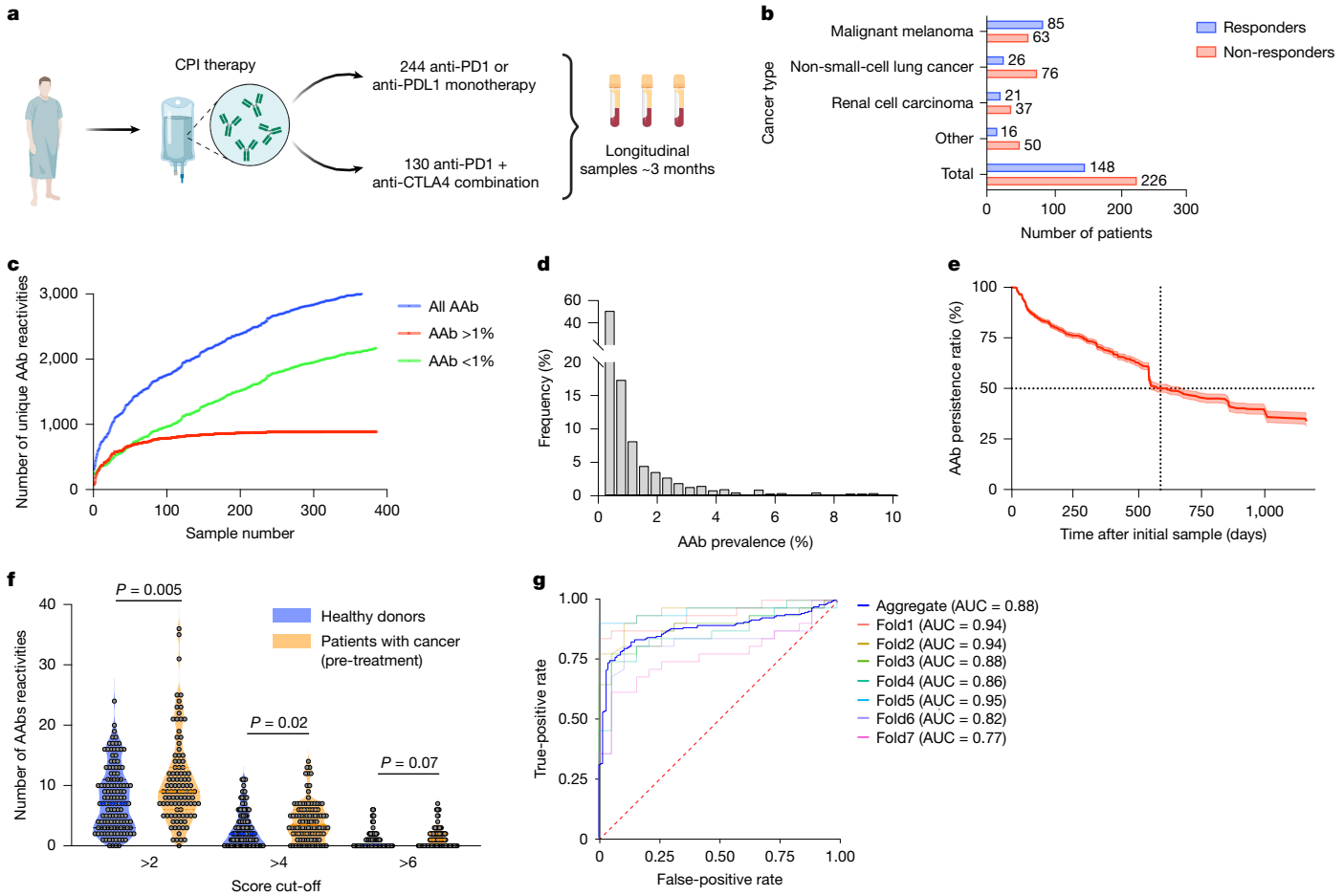

Fig. 1 | Global features of the extracellular AAb reactome in patients treated with CPIs. a, Overview of the screening cohort. Longitudinal plasma samples from 374 patients with cancer treated with CPIs and 131 healthy donors were included in this study. The schematic was created using BioRender (https://BioRender.com/kf2v19o). **b**, Breakdown of cancer types and response status in the patient cohort. **c**, AAb discovery rate analysis. This analysis elucidated the relationship between the cohort size and the identified number of unique AAbs. AAbs are categorized as either 'common' (more than 1%) or 'rare' (less than 1%) on the basis of their frequency within the cohort. **d**, AAb frequency distribution across the cohort. Each bar represents the proportion of AAbs observed at the specified frequency within the cohort. **e**, Kaplan–Meier survival curve representing the persistence of AAbs. Persistence was defined as maintaining a REAP score above 1 in the longitudinal samples. Data are presented as survival probability with 95% confidence intervals. Dashed lines indicate the time points after treatment at which 50% of the AAb reactivity was still detectable. **f**, Comparison of the number of positive total reactivities (REAP score under a different threshold indicated in the figure) in healthy donors and pre-treatment samples from patients. Differences were evaluated using linear regression models adjusting for sex and log-transformed age. **g**, Receiver operating characteristic curve of the ability of the REAP score to discriminate patients from healthy donors by using the Lasso model. AUC, area under the curve.

clinical heterogeneity in response to immunotherapy but could also highlight key pathways for therapeutic modulation in cancer. We thus set out to conduct an 'AAb-wide association study' (AAbWAS) with REAP analogous to a genome-wide association study in a cohort of patients receiving CPIs (Extended Data Fig. 1).

AAbs in patients with cancer treated with CPIs

Using REAP, we profiled plasma samples from a cohort of 374 patients with cancer treated with CPIs (anti-PD1 or anti-PDL1 monotherapy or dual checkpoint blockade with anti-PD1 and anti-CTLA4) and 131 healthy control individuals (Fig. 1a,b and Supplementary Table 1). This cohort contained patients with a wide range of tumour types including melanoma, non-small-cell lung cancer (NSCLC), renal cancer, bladder cancer, head and neck cancers and other cancers, and included extensive longitudinal profiling for most patients treated with CPIs (Extended Data Fig. 2a). As an internal validation of the performance of REAP, we successfully detected the new appearance of PD1 and CTLA4 reactivities that resulted from the administered drugs in patients treated with CPIs (Extended Data Fig. 2b). Overall, we detected an extraordinarily diverse array of 2,922 unique autoreactivities to the exoproteome in the cohort (Fig. 1c). Despite the apparent diversity in autoreactivities, a discovery rate analysis revealed that more autoreactivities remain to be discovered in the population of patients treated with CPIs (Fig. 1c), as most autoreactivities were rare and observed at frequencies of less than 1% (Fig. 1d). Longitudinal analysis of the dynamics of each autoreactivity within individual patients indicated that AAbs were relatively stable, persisted on timescales ranging from several months to years, and were not markedly affected by CPI treatment (Fig. 1e and Extended Data Fig. 2c,d).

We subsequently sought to determine whether patients with cancer exhibited different AAb features compared with healthy donors. By quantifying the total number of autoreactivities per individual, we observed that cancer status was significantly associated with increased numbers of AAbs at REAP reactivity thresholds of more than 2 (effect size of 2.4 additional AAbs, $P = 0.005$) and more than 4 (effect size of 1.0 additional AAb, $P = 0.021$) in pre-treatment samples, after adjusting for age and sex, both of which were also significantly associated with AAb levels (positive association with age and fewer AAbs in male individuals; Extended Data Fig. 2e–h). To determine whether

patients with cancer had distinguishable AAb signatures relative to healthy individuals, we constructed a regularized logistic regression (Lasso) classification model. Under sevenfold cross-validation, the model demonstrated a strong predictive value in differentiating patients with cancer from control donors, with its receiver operating characteristic curve resulting in an average area under the curve of 0.88 (Fig. 1g). In summary, these results indicate that patients with cancer before immunotherapy exhibit an elevated degree of humoral autoimmunity and unique AAb signatures.

AAbs are associated with CPI responses

We next sought to determine whether AAb reactivities were associated with differences in treatment outcomes as assessed by radiographic imaging. We categorized patients who experienced a radiographic complete response or partial response as responders and those with stable disease and progressive disease as non-responders according to their best response at any point in the administered regimen. To infer the contributions of individual autoreactivities to treatment response, we calculated odds ratios for each detected autoreactivity by comparing its occurrence in responders and non-responders (Fig. 2a). Given that patient characteristics can influence treatment responses, we adjusted the odds ratios for several features. We examined the effects of age, sex, tumour type, CPI treatment regimen, tumour PDL1 status, previous treatment with CPIs, plasma lactate dehydrogenase (LDH) levels, tumour stage and Eastern Cooperative Oncology Group performance status (Supplementary Table 2) on the likelihood of treatment response and made adjustments for variables with significant effects (as described in Methods). Ultimately, we detected numerous associations of clinical responses with AAbs that targeted a wide spectrum of antigens, encompassing immunomodulatory receptors and their ligands, cytokines, growth factors and tumour-associated surface antigens (Extended Data Figs. 3 and 4). Although these AAbs appeared to influence CPI response, they were not unique to patients with cancer and exhibited substantial overlap with profiles from other populations analysed in previous REAP studies (Supplementary Tables 3 and 4).

With respect to immunomodulatory pathways, we found numerous AAb responses that targeted co-stimulatory and co-inhibitory proteins (Fig. 2b). In general, we found that antibody responses to co-inhibitory proteins—such as FGL1 (the ligand for LAG3)[22], the TIGIT ligands PVRL1 and PVRL4 (ref. 23) and the CD47 receptor SIRPα[24]—conferred higher odds ratios for treatment response (Fig. 2c). By contrast, AAbs targeting co-stimulatory checkpoints conferred odds ratios of less than 1 (enriched in non-responders). Together, these results suggested that humoral perturbation (that is, disinhibition) of co-inhibitory pathways may have enhanced antitumour immunity driven by CPI, whereas disruption of co-stimulatory pathways hindered effective immunotherapeutic responses.

We also observed associations of AAbs to inflammatory cytokines, including IL-6, IL-17, OSM and IFN-I, with higher odds ratios for response to CPIs (Fig. 2d). To determine whether these antibodies were functional, we assessed their ability to modulate signalling driven by their cytokine antigen targets using ex vivo phosphoflow cytometry signalling assays for IL-6 and OSM. The addition of IgG from patients containing these AAbs, but not from patients that lacked them, inhibited signalling from their respective cytokine targets (Fig. 2e). This finding is consistent with emerging evidence that these pathways drive pathological inflammation in the tumour microenvironment that leads to immunosuppression[25–28].

Given the historical association of tumour-opsonizing antibodies with enhanced patient survival[14,15], we sought to analyse the impact of AAbs to tumour-associated antigens on CPI outcomes. Consistent with previous observations, we found that antibodies to established tumour-associated antigens including MSLN, MET, GPC1, GPC3, CLDN18 and the stress-induced NKG2D ligands ULBP2, ULBP4 and ULBP6 conferred elevated odds ratios for CPI response (Fig. 2f,g).

By contrast, some AAbs were associated with lower odds ratios for CPI response. Two of the most enriched AAbs in non-responders were the BMP receptors BMPR1A and BMPR2, which are co-receptors for the bone morphogenic proteins BMP2, BMP4, BMP7 and GDF5 (ref. 29). These AAbs were detected in approximately 10% of non-responders but in fewer than 1% of either healthy donors or CPI responders (Fig. 2h,i). We biochemically validated these antibodies via ELISA (Fig. 2j) and assessed their functionality using an in vitro BMPR signalling assay, finding that IgG isolated from BMPR AAb$^+$ patients potently inhibited BMP2-induced signalling (Fig. 2k). These results thus suggest that there may be a heretofore unappreciated contribution of BMP pathway function to the efficacy of CPIs.

IFN-I-neutralizing AAbs improve response

AAbs to the IFN-I family were among the most striking associations with CPI responders, conferring odds ratios of response ranging from approximately 2.1 to 6.7 (Fig. 3a). The only exception was IFNβ, in which reactivity was observed in only a single,l non-responding patient. Although reactivity to individual IFN-I proteins was associated with higher odds of response to CPIs, eight patients had AAbs broadly targeting multiple IFN-I proteins. Patients with this broad pattern of reactivity universally responded to CPI therapy (Fig. 3b). To evaluate the functionality of the IFN-I AAbs, we conducted a flow cytometry-based signalling assay in THP-1 cells and found that plasma samples from individuals with broad anti-IFN-I autoreactivity potently inhibited pSTAT1 signalling induced by IFNα2, IFNα4 and IFNα8 (Fig. 3b and Extended Data Fig. 5a). These results thus indicated that neutralization of IFN-I may enhance the therapeutic effect of CPI therapy.

Consistent with this hypothesis was the behaviour of IFN-I AAbs present in non-responders (Fig. 3b). IFN-I AAbs in non-responders targeted individual IFN-I proteins only narrowly and with lower REAP reactivity than seen in responders (Extended Data Fig. 3). Furthermore, plasma samples from patients with reactivity to single IFN-I proteins lacked IFN-I-neutralizing ability (Fig. 3b). As hotspots within the contact interface of IFN-I proteins with the IFNAR subunits are highly conserved[30], the narrow cross-reactivity of IFN-I AAbs in non-responders and their lack of IFN-I neutralization indicates that AAbs in these patients recognize distinct non-receptor-binding epitopes. When we refined our analysis to samples with demonstrated IFN-I-neutralizing activity, we found that the presence of IFN-I-neutralizing ability markedly enhanced the predictive value of these responses, elevating the odds ratio for CPI response to 40.4.

To assess the potential in vivo effects of the IFN-I AAbs detected in our cohort, we conducted immunophenotyping of peripheral blood mononuclear cells (PBMCs) from patients with and without IFN-I AAbs. Previous reports have found that neutralizing IFN-I AAbs are associated with increased frequency of peripheral blood monocytes characterized by high LAIR1 expression[31] and that IFN-I signalling has a crucial role in B cell survival and development[32]. Although most immune subsets were not substantially affected by the presence of IFN-I AAbs, we found that patients with neutralizing IFN-I AAbs demonstrated elevated frequencies of CD14$^+$LAIR1$^+$ monocytes and a reduction in naive B cells (Fig. 3c,d and Extended Data Fig. 5b,c), consistent with previous findings[31,32].

Classically, the IFN-I pathway has been associated with antitumour immune responses, and recombinant IFNα2b is an approved therapy for various malignancies including melanoma[33]. However, recent forward and reverse genetic studies in mice have paradoxically indicated that chronic IFN-I signalling promotes an immunosuppressive tumour microenvironment and contributes to T cell exhaustion[26,34,35]. Our finding that IFN-I pathway-neutralizing AAbs are associated with favourable responses to CPI therapy provides translational support for these

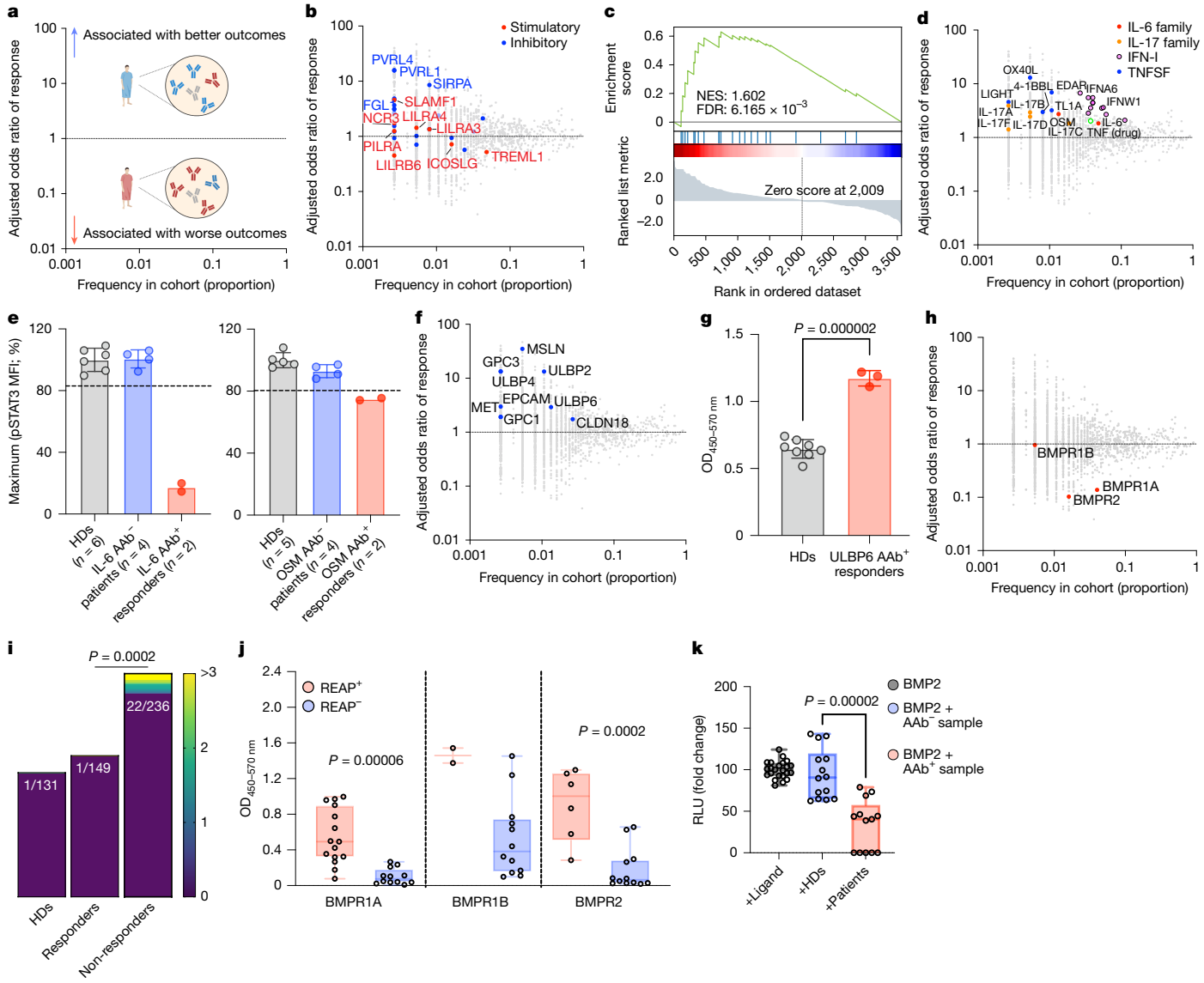

Fig. 2 | Functional AAbs are associated with treatment outcome. a, Conceptual figure for the correlation between AAb odds ratios and treatment outcome. The schematic was created using BioRender (https://BioRender.com/t1qgxor). **b**, Distribution of odds ratios and frequencies for AAbs targeting antigens associated with immune checkpoints. **c**, Gene set enrichment analysis for AAbs to inhibitory immune checkpoints. FDR, false discovery rate; NES, normalized enrichment score. **d**, Distribution of odds ratios and frequencies for AAbs targeting cytokine pathways that elicit pathological inflammation. **e**, Schematic and results of the IL-6 and OSM blocking assay conducted with plasma from healthy donors (HDs; $n = 6$ in the IL-6 assay and $n = 5$ in the OSM assay). $n = 4$ AAb^- patients with cancer and $n = 2$ AAb^+ patients with cancer. Data are presented as mean ± s.d. The dashed line indicates three standard deviations below the average value for AAb^- patients. MFI, mean fluorescence intensity. **f**, Distribution of odds ratios and frequencies for AAbs targeting tumour-associated antigens. **g**, ELISA validation of anti-ULBP6 AAbs. Data are presented as mean ± s.d. Significance was assessed by a two-sided Student's *t*-test. $n = 8$ healthy donors and $n = 3$ ULBP6 AAb^+ responders. **h**, Distribution of odds ratios and frequencies for AAbs targeting the BMP2–BMP4 signalling pathway. **i**, Heatmaps of REAP scores for BMPR1A or BMPR2 receptors in responders, non-responders and healthy donors. Significance was assessed by a two-sided Mann–Whitney *U*-test. **j**, ELISA validation of AAbs to BMPR1A and BMPR2 receptors. Data are presented as boxplots, where the centre line indicates the median, the box bounds represent the 25th and 75th percentiles (interquartile range), and the whiskers represent the minimum and maximum values. Individual data points are overlaid. Significance was assessed by a two-sided Student's *t*-test. $n = 15$ $BMPR1A$ AAb^+ patients, $n = 2$ $BMPR1B$ AAb^+ patients, $n = 6$ $BMPR2$ AAb^+ patients and $n = 12$ AAb^- patients. OD, optical density. **k**, Results of the BMP2-blocking assay conducted with plasma from healthy donors ($n = 14$) and patients with cancer harbouring BMPR1A or BMPR2 AAbs validated by ELISA ($n = 13$). Data are presented as boxplots, defined as in panel **j**. Significance was assessed by a two-sided Student's *t*-test. RLU, relative light units.

preclinical findings. To confirm that pharmacological blockade of IFN-I signalling enhances CPI therapy, we sought to model the effect of the neutralizing IFN-I AAbs in mouse tumour models. We thus evaluated the impact of combining monoclonal antibodies that block IFNAR1 or broadly neutralize mouse IFN-I proteins with CPIs in the syngeneic B16F10 and CT26 tumour models (Fig. 3e). In both models, we observed that the addition of an IFN-I pathway-blocking antibody enhanced the efficacy of combined CPI therapy (anti-PD1 and anti-CTLA4; Fig. 3f,g and Extended Data Fig. 5d). In the case of the B16F10 model, which is highly resistant to CPIs, tumour growth inhibition was evident only when IFN-I blockade was present. In the case of CT26, a CPI-responsive model, the addition of IFN-I pathway inhibition resulted in significantly more rapid tumour clearance. These results are consistent with recent reports in other preclinical models that demonstrated that IFN pathway antagonists including JAK inhibitors and anti-IFNAR antibodies could augment the efficacy of CPIs[36,37].

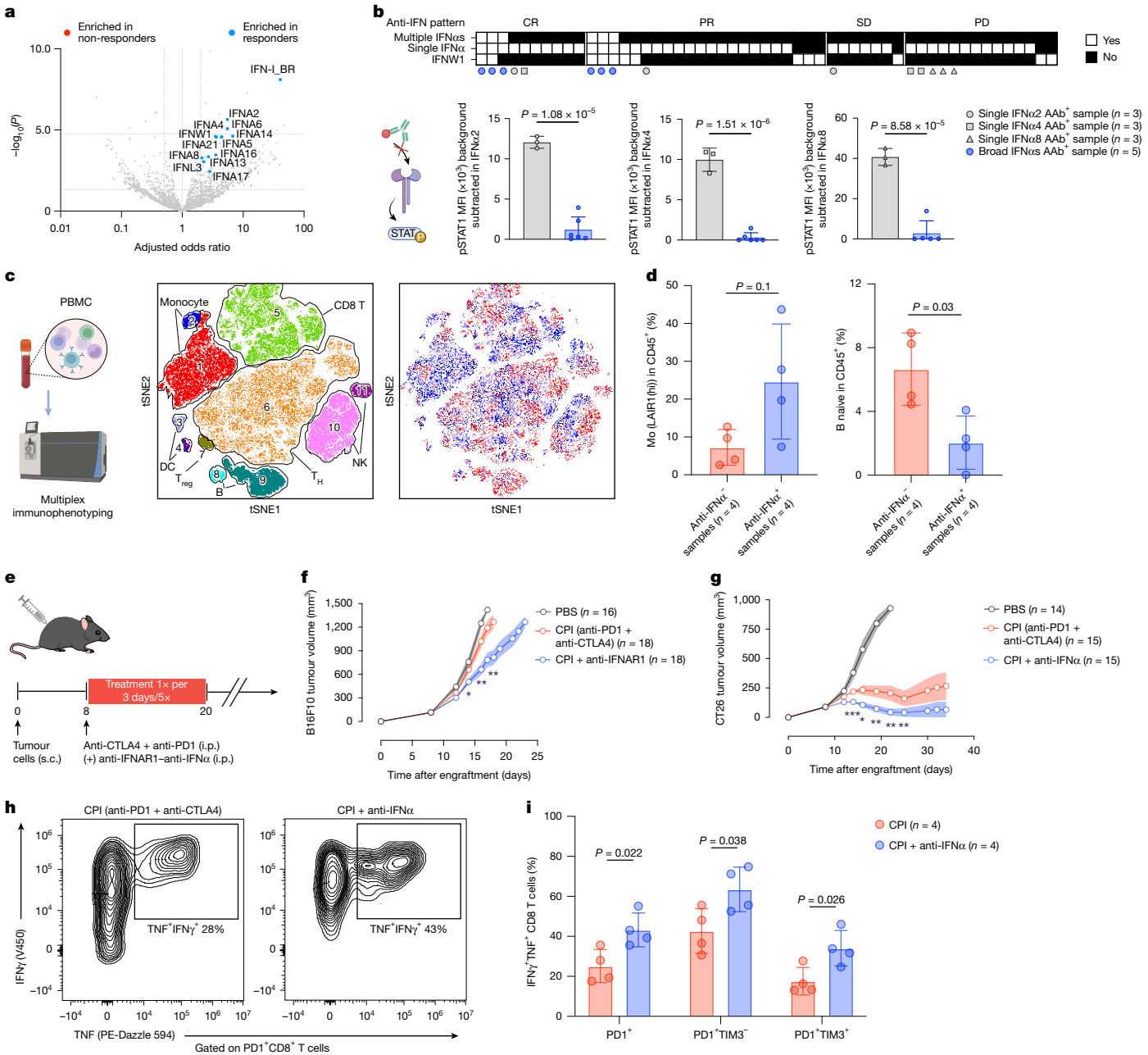

Fig. 3 | Anti-IFN-I AAbs are enriched in CPI responders. a, Volcano plot showing the adjusted odds ratio and the log-transformed *P* value of AAbs in responders versus non-responders. IFN-I_BR (broadly reactive) indicates more than 1 IFN-I reactivity in a sample. The dashed lines represent $P = 0.05$ (lower, not adjusted) and Bonferroni significance threshold at $P = 0.000017$ (upper, for reference). Significance was assessed by two-sided Firth logistic regression, as detailed in Methods. **b**, IFNα2, IFNα4 and IFNα8 signalling assays were conducted in the presence of plasma from patients with REAP reactivity to individual or multiple IFN-I proteins. All IFN-I-reactive individuals in the metacohort are shown in the table, and samples used in the assay are indicated with symbols. Data are presented as mean ± s.d. Significance was assessed by two-sided Student's *t*-test. CR, complete response; PD, progressive disease; PR, partial response; SD, stable disease. **c**, Schematic and results of immunoprofiling of PBMCs from patients matched by clinical status to evaluate the in vivo effects of IFN-I AAbs. Results are visualized in a tSNE plot with assigned cell types. Red indicates IFN-I AAb-positive samples, and blue indicates negative samples. NK, natural killer; T_H, helper T; T_{reg}, regulatory T. **d**, Comparison of LAIR1$^+$ monocytes and naive B cell frequency in IFN-I AAb-positive or AAb-negative samples. Data are presented as mean ± s.d. Significance was assessed by two-sided Wilcoxon rank-sum test. **e**, Schematic of the mouse tumour study evaluating the synergistic effects of CPI treatment and IFNα pathway blockade. i.p., intraperitoneal; s.c., subcutaneous. The schematics in panels **b**,**c**,**e** were created using BioRender (https://BioRender.com/q2khgqp; https://BioRender.com/vkohdqt; https://BioRender.com/7at1lmf). **f**,**g**, Mean tumour growth curve for mice bearing B16F10 (**f**) or CT26 (**g**) tumours under different treatment conditions. The figures represent pooled results from two independent experiments per tumour model. Data are presented as mean ± s.e.m. Significance was assessed by two-sided Student's *t*-test. For B16F10, $P = 0.047$ (day 14), 0.0048 (day 16) and 0.0046 (day 18). For CT26, $P = 0.0004$ (day 14), 0.013 (day 16), 0.003 (day 19), 0.0026 (day 22) and 0.0029 (day 25). **h**,**i**, Representative flow plots (**h**) and relative ratio (**i**) of polyfunctional CD8$^+$PD1$^+$ T cells in different treatment groups. Data points in panel **i** represent individual tumours measured in unicate with four mice per group. Data are presented as mean ± s.d. Significance was assessed by two-way ANOVA.

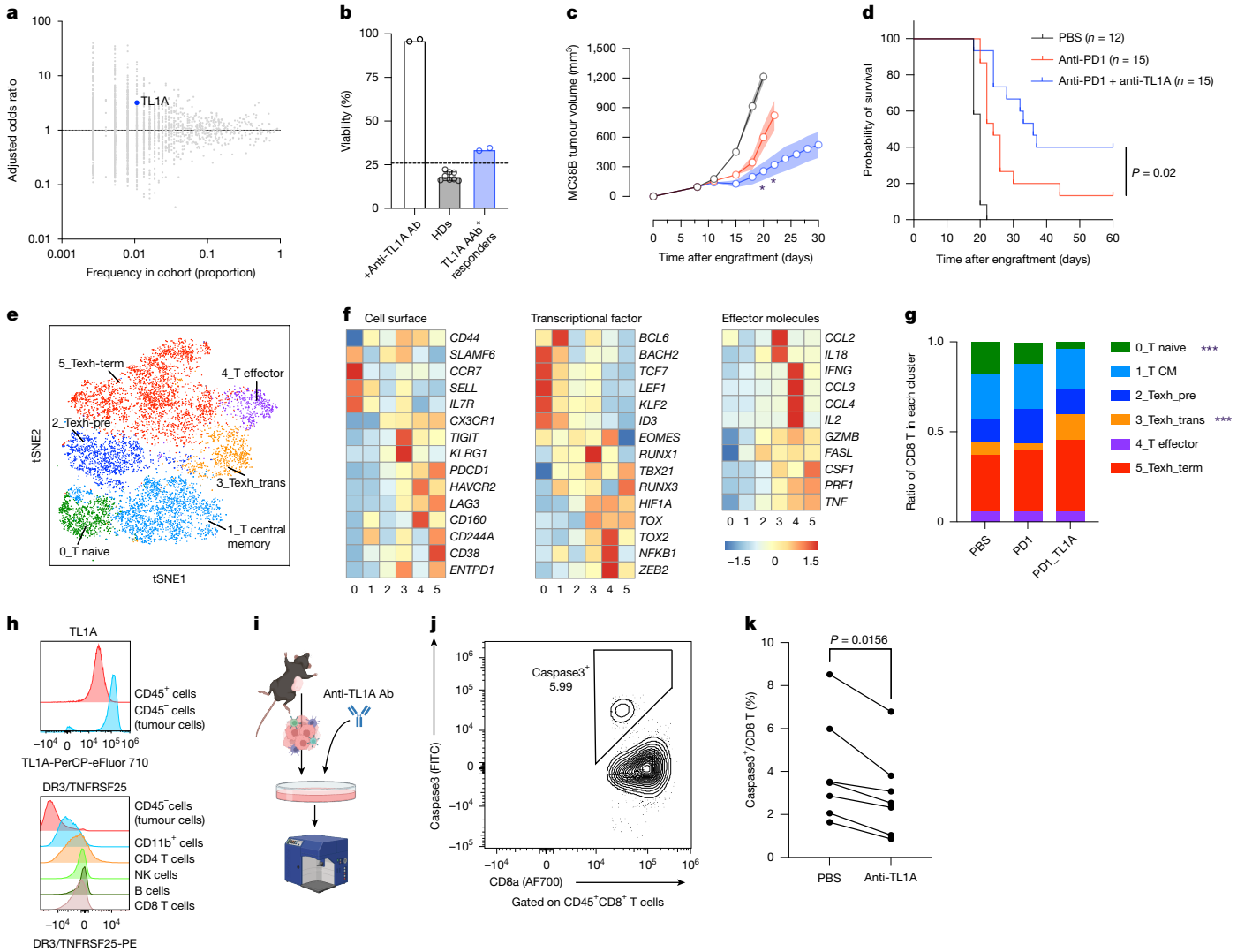

Fig. 4 | Anti-TL1A AAbs are enriched in CPI responders. a, Distribution of odds ratios and frequencies for anti-TL1A AAbs. The dashed line indicates an odds ratio of 1. **b**, Schematic and results of the TL1A-blocking assay conducted with purified IgG from healthy donors (controls; $n = 8$) and patients with cancer harbouring anti-TL1A AAbs ($n = 2$). Data are presented as mean ± s.d. The dashed line indicates three standard deviations above the average value of healthy donors. **c**,**d**, Results for the mouse MC38 tumour study under different treatment conditions. The figures represent pooled results from two independent experiments, with the number of animals per group indicated in the legend. Representative mean tumor growth is shown (**c**). Data are presented as mean ± s.e.m. $P = 0.0341$ (day 20) and 0.0216 (day 22). Significance was assessed by a two-sided Student's *t*-test (**c**). Kaplan–Meier survival curves are also displayed (**d**). Significance was assessed by the log-rank test. **e**, tSNE projection showing $CD8^+$ T cells present in MC38 tumours coloured by cluster. A full description of single-cell experimental and analysis procedures are provided in Methods. Term, terminal; Texh, exhausted T. **f**, Heatmap showing normalized mean expression of the curated gene list in intratumoural $CD8^+$ T cell clusters from panel **e**. **g**, Barplot showing frequency of T cells within clusters of interests in different treatment groups. Significance was assessed by a two-sided Fisher's exact test. CM, central memory. **h**, Representative histogram assessing staining for TL1A and its receptor TNFRSF25 by flow cytometry of tumour cells and intratumoural $CD45^+$ cells. **i**–**k**, Schematic (**i**) and results (**j**,**k**) of the apoptosis assay of tumour-infiltrating lymphocytes. Paired samples from the same tumour with and without anti-TL1A treatment are connected with lines. Significance was assessed by a paired two-sided Wilcoxon rank-sum test. The experiment was conducted in unicate with tumour samples from seven mice. The schematic in panel **i** was created using BioRender (https://BioRender.com/j6pw9ap).

To probe the immunological effects of IFN-I blockade, we immunophenotyped tumour-infiltrating lymphocytes in CT26 tumours from mice treated with CPI, with and without IFN-I antibody blockade. Of note, we observed an increased proportion of polyfunctional $CD8^+PD1^+$ T cells that produced both IFNγ and TNF in tumours from mice treated with a pan-IFN-I-neutralizing antibody (Fig. 3h and Extended Data Fig. 5e,f). This increase in effector functionality was exhibited by both $PD1^+TIM3^+$ (double-positive) cells and the $PD1^+TIM3^-$ (single-positive) population (Fig. 3i and Extended Data Fig. 5e,f), indicating a broad increase in functionality across T cell maturation and exhaustion states.

AAb response reveals TL1A as a CPI barrier

Given the theme that AAbs that neutralize inflammatory cytokines (that is, anti-IFN-I, anti-IL-6 and anti-IL-17) appear to enhance the efficacy of CPIs, we sought to identify additional examples in pathways that had not been previously implicated in CPI biology. To that end, the TNF superfamily member TL1A (also known as TNFSF15) caught our attention owing to its increased odds ratio (OR of 3.2) and prevalence in approximately 1% of patients (Fig. 4a). To assess the functionality of these AAbs, we performed a TL1A functional assay and found that purified IgG from CPI responders with anti-TL1A AAbs could attenuate

TL1A-induced apoptosis of TF-1 erythroblast cells (Fig. 4b). We then evaluated the impact of antibody-mediated TL1A blockade in combination with anti-PD1 in the syngeneic MC38 mouse tumour model, finding that combined TL1A and PD1 blockade resulted in enhanced antitumour efficacy relative to anti-PD1 alone (Fig. 4c,d).

To investigate the mechanism underlying the effect of blocking TL1A in the context of CPI, we performed single-cell RNA sequencing of MC38 tumours after treatment with PBS, anti-PD1, or anti-PD1 and anti-TL1A (Extended Data Fig. 6). The most striking differences were evident in CD8 T cells, with the other CD45$^+$ immune cells showing few changes (Extended Data Fig. 7a–e). Analysis of the CD8a$^+$ cluster revealed six subclusters that fit with the previous classification for naive, central memory, effector-like, and pre-exhausted, trans-exhausted or terminal-exhausted T cells established in a chronic lymphocytic choriomeningitis virus (LCMV) infection model[38] (Fig. 4e,f and Extended Data Fig. 8). Consistent with CPI therapy driving expansion and maturation of activated lymphocytes, the anti-PD1 and anti-PD1–anti-TL1A groups demonstrated increases in the frequencies of exhausted CD8 populations with decreases in frequencies of naive CD8 cells relative to PBS. In comparison with the anti-PD1 group, the combined anti-PD1–anti-TL1A treatment group showed increased frequencies of more differentiated exhausted T cells, particularly in cluster_3 trans-exhausted CD8 T cells (Fig. 4g).

As transcripts for TL1A and its receptor DR3 (TNFRSF25) were not detected in any of the clusters, it was not possible to infer cell–cell interactions mediating the effects of TL1A from the single-cell RNA sequencing datasets. We thus performed flow cytometry on dissociated MC38 tumours, finding that tumour cells were the highest expressors of TL1A, whereas DR3 was broadly expressed on various immune cells (Fig. 4h). Considering that tumour expression of other TNFSF members such as FASL has been proposed to mediate apoptosis of antitumour lymphocytes[39] and that the TL1A–DR3 pathway has been implicated in T cell apoptosis during thymocyte negative selection[40], we hypothesized that TL1A expressed by tumour cells might similarly elicit apoptosis of anti-PD1 treatment-sensitized CD8 T cells. We thus performed an ex vivo assay in which we cultured dissociated tumours from anti-PD1-treated mice in the presence or absence of TL1A-neutralizing antibodies (Fig. 4i). Consistent with our hypothesis, anti-TL1A treatment resulted in a decrease in caspase3$^+$ apoptotic CD8 cells (Fig. 4j,k and Extended Data Fig. 7f). These results thus indicate that TL1A–DR3 interactions may extend beyond central tolerance to modulate apoptosis of peripheral T cells, including the tumour-infiltrating lymphocytes that mediate the efficacy of CPIs.

AAb associations across tumour types

Because they target the immune system, CPIs have a broad spectrum of clinical activity across a wide range of tumour types. However, different tumour types vary greatly in their intrinsic immunogenicity. We thus sought to address whether AAb associations with treatment response varied between tumour types and calculated odds ratios of clinical response for AAbs for the three largest tumour types in the cohort: melanoma (n = 150), NSCLC (n = 102) and renal cell carcinoma (n = 58). Given differences in clinicopathological features between these tumour types, we tailored the odds ratio adjustments to align with known variables in predicting CPI response for each tumour type (Supplementary Table 2 and described in Methods). Furthermore, because of the substantially reduced sizes of these subcohorts relative to the larger metacohort, we focused on a set of responses with significant effects on odds ratio that were present in a larger fraction of patients (more than 5% prevalence), namely anti-IFN-I, anti-IFN-III and anti-BMPR1A–BMPR2.

For these AAbs, we noted a striking concordance in the directionality and magnitude of the odds ratios for CPI response between tumour types and the pan-cancer metacohort (Extended Data Fig. 9a). AAb reactivities to IFN-I were consistently associated with increased odds ratios for CPI response, and BMPR1A–BMPR2 were consistently associated with sharply decreased odds ratios. However, an interesting case can be seen with AAbs towards members of the IFN-III family. In our cohorts, we detected AAbs to IL-28A (encoded by *IFNL2*) and IL-28B (encoded by *IFNL3*), which were not strongly associated with immunotherapeutic responses in melanoma or renal cell carcinoma, but showed odds ratios of more than 5 in NSCLC (Extended Data Fig. 9b). In fact, for NSCLC, the anti-IFN-III odds ratios were higher than for anti-IFN-I. This is consistent with the distribution of IFN-III expression, which is higher in the lung and other mucosal surfaces that are at increased risk of viral exposure[41]. Accordingly, analysis of The Cancer Genome Atlas transcript expression data indicates that IFN-III expression is far more prevalent in lung cancers than in melanoma or kidney cancers[42] (Extended Data Fig. 9c). This finding indicates that differences in the local tissue environments between tumours may influence the effects of AAbs on treatment response.

As an additional means of cross-validation of our results, we also compared response odds ratios for the same AAb reactivities between samples derived from the Yale cohort with samples from the MT Group commercial biorepository. As with the tumour-type analysis, the directionality and magnitude of the odds ratios for CPI response were similar for both cohorts and consistent with the overall metacohort (Extended Data Fig. 9d).

AAbs and immune-related adverse events

CPI therapy is characterized by a wide range of organ-specific inflammatory effects called immune-related adverse events (irAEs)[43]. We therefore investigated whether AAbs before or elicited by CPIs could contribute to the development of irAEs. In our cohort, the primarily observed irAEs were thyroiditis or hypothyroidism, hypophysitis, enteritis or colitis, pancreatitis and hepatitis (Extended Data Fig. 10). Consistent with previous studies[44,45], we found that the severity of irAEs was positively associated with the antitumour response to therapy (Fig. 5a). Contrary to our expectations, we found that anti-PD1 or anti-PDL1 monotherapy did not cause a net increase in the total number of AAbs. The addition of anti-CTLA4 for dual checkpoint blockade resulted in a modest net increase in reactivities, with an average of one new autoreactivity gained per patient (Fig. 5b). Similarly, we did not observe a relationship between the prevalence or severity of irAEs and the number of autoreactivities in patients (Fig. 5c).

Although we did not observe readily apparent global associations of AAbs and irAEs, we performed analyses to determine whether individual autoreactivities were associated with specific irAE types (Fig. 5d). Although there were few irAE-specific reactivities, AAbs to the G-protein-coupled receptor QRFPR stood out owing to their specificity for hypophysitis coupled with the tissue-specific expression pattern of QRFPR within the hypothalamus[46]. Of note, approximately 11% (4 of 35) of patients with hypophysitis had AAbs to QRFPR, whereas these AAbs were absent in patients with other irAEs, in patients without irAEs or in healthy donors (Fig. 5e,f). We confirmed the binding of these AAbs using ELISA (Fig. 5g) and determined their subtypes to be the IgG1 and IgG3 subclasses, which exhibit the highest degree of antibody effector functionality (Fig. 5h). QRFPR AAbs were present in pre-treatment samples for two of the four QRFPR AAb-positive patients, whereas the other two patients developed them after CPI administration (Fig. 5i).

Discussion

Through exoproteome-wide AAb profiling, we found that patients with cancer have a remarkably diverse AAb reactome. Despite analysing nearly 400 patients and identifying AAb reactivities against nearly 3,000 proteins, our study did not fully elucidate the spectrum of extracellular autoreactivities within this population. These results

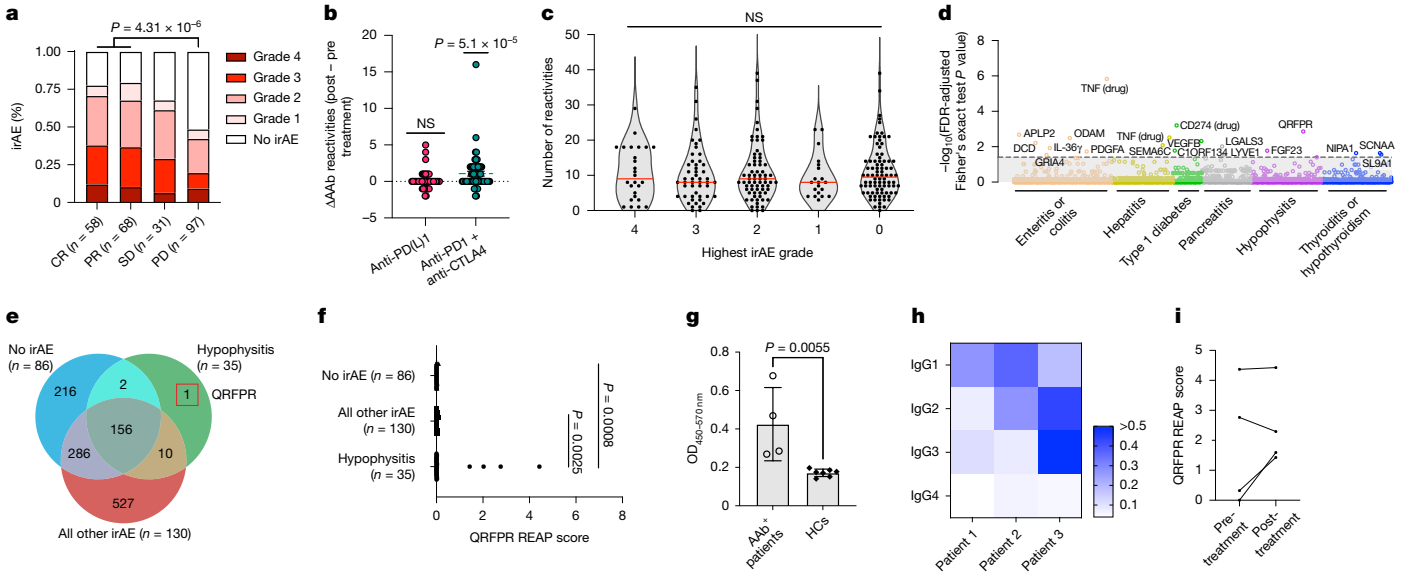

Fig. 5 | Anti-QRFPR AAbs are associated with CPI-induced hypophysitis. **a**, Distribution of severity grades for irAEs among patients based on treatment outcomes. In cases in which multiple irAEs were observed in a patient, the most severe grade was selected for the analysis. Significance was assessed by a two-sided Fisher's exact test. **b**, Alteration in the count of AAbs between pre-treatment and the first post-treatment samples. $n = 44$ for the anti-PD(L)1 group, and $n = 58$ for the anti-PD1 + anti-CTLA4 group. Significance was assessed using a two-sided one-sample Wilcoxon signed-rank test. NS, not significant. The dashed line indicates a value of 0. **c**, Comparison of AAb counts across patients based on irAE severity levels. For patients experiencing multiple irAEs, the analysis considered only the highest severity grade. Significance was assessed by a two-sided Mann–Whitney *U*-test. Data are presented as dots, with the mean value indicated by the red line. NS, not significant. **d**, Manhattan plot of false discovery rate (FDR)-adjusted *P* values from Fisher's exact tests comparing the REAP score for AAbs between patients stratified by irAEs. Only AAbs that were more prevalent in the specified disease group were tested. TNF reactivities were the result of administration of anti-TNF therapy for treatment of irAEs, and CD274 reactivity was the result of the administered CPI (anti-PDL1). Detailed comparison procedures can be found in Methods. **e**, Venn diagram depicting the distribution and overlap of AAbs across the indicated patient categories. Only AAbs with a REAP score above 1 in at least two patients were included for comparison. **f**, REAP scores for anti-QRFPR AAbs in the indicated patient categories. Significance was assessed by two-sided Wilcoxon rank-sum test. **g**, ELISA validation of anti-QRFPR AAbs. Data are presented as mean ± s.d. Significance was assessed by a paired two-sided Student's *t*-test. **h**, Heatmap of ELISA reactivity examining the isotypes of anti-QRFPR AAbs. **i**, REAP scores for anti-QRFPR AAbs in the positive patients between pre-treatment and post-treatment samples ($n = 4$). Longitudinal samples from the same patient are connected with lines.

thus indicate that at a population level, AAbs have the potential to functionally sample a vast fraction of the exoproteome. Indeed, the effect of individual AAbs on treatment effectiveness underscores a more profound interplay between humoral immunity and checkpoint immunotherapy than previously recognized.

With this perspective in mind, our results highlight the value of conducting AAbWAS[20] that are analogous to genome-wide association studies to identify key biological pathways that contribute to phenotype (in this case, response to CPI therapy). Our findings reinforce the importance of established mechanisms of checkpoint blockade resistance, including the detrimental effects of cytokines that foster an immunosuppressive tumour microenvironment, such as IL-6, IL-17 and IFN-I[25–28]. However, they also identify new potential players in tumour immunity, including a suppressive role of TL1A on tumour immunity and a potential requirement for BMPR1A–BMPR2 pathway activity for optimal immunotherapeutic outcomes. Although some of these hits are rare, their potential impact may prove substantial. This mirrors the role of rare genetic variants, where even low-frequency mutations, such as those in PCSK9 in lipid homeostasis[47], have highlighted key biological pathways. Likewise, rare AAb hits, such as anti-TL1A in our study, can uncover novel, therapeutically actionable pathways for improving CPI response in a broader patient population.

AAbWAS also provides insights into potential therapeutic strategies. AAbs can be conceptualized as natural biologic drugs in that they are human antibodies that target human proteins. The potential efficacy of intentionally targeting a particular protein can be inferred from the outcomes of patients that naturally harbour AAbs to the same target. Likewise, analysing AAb effects can elucidate optimal therapeutic mechanisms, offering insights into how targeting specific AAbs might inform treatment strategies. AAbs that enhance therapeutic responses essentially provide a template for the design of new biologic therapies that mimic their effects (for example, blockade of IFN-I or TL1A). Conversely, AAbs that impair treatment outcomes illuminate the negative ramifications of disrupting certain pathways, suggesting that counteracting these effects could guide therapeutic design (for example, enhancing rather than inhibiting BMPR1A–BMPR2 signalling). For some treatment-enhancing AAb reactivities, analogous FDA-approved therapeutics already exist for other indications, highlighting the potential for repurposing these drugs for cancer immunotherapy. A salient example from our data can be seen with IFN-I neutralizing AAbs and the lupus therapeutic anifrolumab, which blocks IFNAR[48]. The improved CPI outcomes in patients with IFN-I AAbs, together with the preclinical validation of IFN-I blockade in mouse models of CPI therapy[26,34], provide a strong basis for future clinical trials exploring the combination of anifrolumab with CPIs.

The putatively beneficial effect of anti-IFN-I AAbs on CPI response also highlight the pleiotropic and even dichotomous effects that AAbs can exert on health outcomes. In COVID-19, anti-IFN-I AAbs are present in approximately 10% of severe cases and have been estimated to increase the odds of death by 20–200-fold[17]. However, anti-IFN-I AAbs have also been described in other populations including systemic lupus erythematosus (10–25% of cases)[49] and the general population (approximately 0.5–4% prevalence, depending on age)[50]. In our cohort, patients with anti-IFN-I AAbs were 71% male individuals with an average age of 75 years, closely resembling the demographics of patients with severe acute COVID-19 with these AAbs. It is thus interesting to consider

whether the anti-IFN-I AAbs associated with better CPI responses share a similar origin to the anti-IFN-I AAbs in severe COVID-19.

In contrast to its effect on the efficacy of CPI, we did not detect strong associations with extracellular autoreactivities and irAEs. There was no clear relationship between the number of REAP autoreactivities and irAE prevalence or severity, and there were few associations between individual reactivities and specific irAEs. The absence of a correlation might indicate that most irAEs are driven by cellular, rather than humoral, autoimmunity[51]. Alternatively, REAP might not sensitively detect AAbs responsible for irAEs, or this observation could reflect the rarity and specificity of AAbs in mediating individual adverse events. Larger cohorts might be needed to elucidate the roles of AAbs and irAEs. Nevertheless, we did detect previously undescribed AAbs to the hypothalamus-expressed GPCR QRFPR in approximately 11% of patients treated with CPIs who developed hypophysitis. The dynamics of these AAbs was surprisingly divergent, with half of the patients developing them after CPI therapy and the other half harbouring them before treatment. These results thus suggest that some patients who develop irAEs may have subclinical autoreactivity that is unmasked by CPI therapy, whereas in other cases, autoimmune responses associated with irAEs are formed de novo after CPI administration.

Overall, our results offer preliminary insights into the landscape of AAb reactivities in patients treated with CPIs and the influence they may exert on clinical outcomes. However, there are key limitations that should be considered. The first limitation relates to statistical power. Although we detected thousands of extracellular reactivities within our cohort, analysis of the frequency distribution of AAbs indicated that most autoreactivities are relatively rare, present in less than 1% of individuals. Although the purpose of our studies was hypothesis generating, the observation that most autoreactivities are rare suggests the need for larger cohorts to detect clinically relevant AAb associations. The second limitation relates to determining the flow of causality between AAbs and clinical outcomes. Given that AAbs are themselves products of the immune response, their presence may not always be an independent causal factor in CPI response phenotypes. Rather, AAbs may represent a biomarker of an underlying immune state with an altered propensity for response to immunotherapy. Here we attempted to address this possibility by evaluating mouse AAb 'surrogates' (that is, antibodies with matched function to human AAbs) in preclinical models. These functional studies indicated that, in the case of AAbs to IFN-I and TL1A, these AAbs are probably mechanistically associated with response. Ultimately, validating the causal effects of AAbs on therapeutic outcomes necessitates clinical studies that either aim to modulate the levels of treatment-inhibiting AAbs or seek to emulate — and potentially surpass — the effects of treatment-enhancing AAbs with targeted therapeutics.

Online content

Any methods, additional references, Nature Portfolio reporting summaries, source data, extended data, supplementary information, acknowledgements, peer review information; details of author contributions and competing interests; and statements of data and code availability are available at https://doi.org/10.1038/s41586-025-09188-4.

1. Sharma, P. et al. The next decade of immune checkpoint therapy. *Cancer Discov.* **11**, 838–857 (2021).
2. Kim, T. K., Vandsemb, E. N., Herbst, R. S. & Chen, L. Adaptive immune resistance at the tumour site: mechanisms and therapeutic opportunities. *Nat. Rev. Drug Discov.* **21**, 529–540 (2022).
3. Wang, E. Y. et al. High-throughput identification of autoantibodies that target the human exoproteome. *Cell Rep. Methods* **2**, 100172 (2022).
4. Larkin, J. et al. Five-year survival with combined nivolumab and ipilimumab in advanced melanoma. *N. Engl. J. Med.* **381**, 1535–1546 (2019).
5. Sade-Feldman, M. et al. Defining T cell states associated with response to checkpoint immunotherapy in melanoma. *Cell* **175**, 998–1013.e20 (2018).
6. Meylan, M. et al. Tertiary lymphoid structures generate and propagate anti-tumor antibody-producing plasma cells in renal cell cancer. *Immunity* **55**, 527–541.e5 (2022).
7. Mazor, R. D. et al. Tumor-reactive antibodies evolve from non-binding and autoreactive precursors. *Cell* **185**, 1208–1222.e21 (2022).
8. Cabrita, R. et al. Tertiary lymphoid structures improve immunotherapy and survival in melanoma. *Nature* **577**, 561–565 (2020).
9. Helmink, B. A. et al. B cells and tertiary lymphoid structures promote immunotherapy response. *Nature* **577**, 549–555 (2020).
10. Petitprez, F. et al. B cells are associated with survival and immunotherapy response in sarcoma. *Nature* **577**, 556–560 (2020).
11. Rivera, A., Chen, C. C., Ron, N., Dougherty, J. P. & Ron, Y. Role of B cells as antigen-presenting cells in vivo revisited: antigen-specific B cells are essential for T cell expansion in lymph nodes and for systemic T cell responses to low antigen concentrations. *Int. Immunol.* **13**, 1583–1593 (2001).
12. Bruno, T. C. et al. Antigen-presenting intratumoral B cells affect CD4$^+$ TIL phenotypes in non-small cell lung cancer patients. *Cancer Immunol. Res.* **5**, 898–907 (2017).
13. Cui, C. et al. Neoantigen-driven B cell and CD4 T follicular helper cell collaboration promotes anti-tumor CD8 T cell responses. *Cell* **184**, 6101–6118.e13 (2021).
14. Kotera, Y., Fontenot, J. D., Pecher, G., Metzgar, R. S. & Finn, O. J. Humoral immunity against a tandem repeat epitope of human mucin MUC-1 in sera from breast, pancreatic, and colon cancer patients. *Cancer Res.* **54**, 2856–2860 (1994).
15. Disis, M. L. et al. High-titer HER-2/neu protein-specific antibody can be detected in patients with early-stage breast cancer. *J. Clin. Oncol.* **15**, 3363–3367 (1997).
16. Ludwig, R. J. et al. Mechanisms of autoantibody-induced pathology. *Front. Immunol.* **8**, 603 (2017).
17. Bastard, P. et al. Autoantibodies against type I IFNs in patients with life-threatening COVID-19. *Science* **370**, eabd4585 (2020).
18. Wang, E. Y. et al. Diverse functional autoantibodies in patients with COVID-19. *Nature* **595**, 283–288 (2021).
19. Britschgi, M. et al. Neuroprotective natural antibodies to assemblies of amyloidogenic peptides decrease with normal aging and advancing Alzheimer's disease. *Proc. Natl Acad. Sci. USA* **106**, 12145–12150 (2009).
20. Jaycox, J. R., Dai, Y. & Ring, A. M. Decoding the autoantibody reactome. *Science* **383**, 705–707 (2024).
21. Dimitrov, J. D. & Lacroix-Desmazes, S. Noncanonical functions of antibodies. *Trends Immunol.* **41**, 379–393 (2020).
22. Wang, J. et al. Fibrinogen-like protein 1 is a major immune inhibitory ligand of LAG-3. *Cell* **176**, 334–347.e12 (2019).
23. Yu, X. et al. The surface protein TIGIT suppresses T cell activation by promoting the generation of mature immunoregulatory dendritic cells. *Nat. Immunol.* **10**, 48–57 (2009).
24. Jaiswal, S. et al. CD47 is up-regulated on circulating hematopoietic stem cells and leukemia cells to avoid phagocytosis. *Cell* **138**, 271–285 (2009).
25. Hailemichael, Y. et al. Interleukin-6 blockade abrogates immunotherapy toxicity and promotes tumor immunity. *Cancer Cell* **40**, 509–523.e6 (2022).
26. Benci, J. L. et al. Tumor interferon signaling regulates a multigenic resistance program to immune checkpoint blockade. *Cell* **167**, 1540–1554.e12 (2016).
27. Vitiello, G. A. & Miller, G. Targeting the interleukin-17 immune axis for cancer immunotherapy. *J. Exp. Med.* **217**, e20190456 (2020).
28. Huseni, M. A. et al. CD8$^+$ T cell-intrinsic IL-6 signaling promotes resistance to anti-PD-L1 immunotherapy. *Cell Rep. Med.* **4**, 100878 (2023).
29. Salazar, V. S., Gamer, L. W. & Rosen, V. BMP signalling in skeletal development, disease and repair. *Nat. Rev. Endocrinol.* **12**, 203–221 (2016).
30. Thomas, C. et al. Structural linkage between ligand discrimination and receptor activation by type I interferons. *Cell* **146**, 621–632 (2011).
31. van der Wijst, M. G. P. et al. Type I interferon autoantibodies are associated with systemic immune alterations in patients with COVID-19. *Sci. Transl. Med.* **13**, eabh2624 (2021).
32. Hamilton, J. A. et al. Endogenous interferon-β regulates survival and development of transitional B cells. *J. Immunol.* **199**, 2618–2623 (2017).
33. Antonelli, G., Scagnolari, C., Moschella, F. & Proietti, E. Twenty-five years of type I interferon-based treatment: a critical analysis of its therapeutic use. *Cytokine Growth Factor Rev.* **26**, 121–131 (2015).
34. Benci, J. L. et al. Opposing functions of interferon coordinate adaptive and innate immune responses to cancer immune checkpoint blockade. *Cell* **178**, 933–948.e14 (2019).
35. Reticker-Flynn, N. E. et al. Lymph node colonization induces tumor-immune tolerance to promote distant metastasis. *Cell* **185**, 1924–1942.e23 (2022).
36. Mathew, D. et al. Combined JAK inhibition and PD-1 immunotherapy for non–small cell lung cancer patients. *Science* **384**, eadf1329 (2024).
37. Zak, J. et al. JAK inhibition enhances checkpoint blockade immunotherapy in patients with Hodgkin lymphoma. *Science* **384**, eade8520 (2024).
38. Giles, J. R. et al. Shared and distinct biological circuits in effector, memory and exhausted CD8$^+$ T cells revealed by temporal single-cell transcriptomics and epigenetics. *Nat. Immunol.* **23**, 1600–1613 (2022).
39. Zhu, J., Petit, P.-F. & Van den Eynde, B. J. Apoptosis of tumor-infiltrating T lymphocytes: a new immune checkpoint mechanism. *Cancer Immunol. Immunother.* **68**, 835–847 (2019).
40. Wang, E. C. Y. et al. DR3 regulates negative selection during thymocyte development. *Mol. Cell. Biol.* **21**, 3451–3461 (2001).
41. Wack, A., Terczyńska-Dyla, E. & Hartmann, R. Guarding the frontiers: the biology of type III interferons. *Nat. Immunol.* **16**, 802–809 (2015).
42. Tang, Z. et al. GEPIA: a web server for cancer and normal gene expression profiling and interactive analyses. *Nucleic Acids Res.* **45**, W98–W102 (2017).
43. Postow, M. A., Sidlow, R. & Hellmann, M. D. Immune-related adverse events associated with immune checkpoint blockade. *N. Engl. J. Med.* **378**, 158–168 (2018).
44. de Moel, E. C. et al. Autoantibody development under treatment with immune-checkpoint inhibitors. *Cancer Immunol. Res.* **7**, 6–11 (2019).
45. Weber, J. S. et al. Safety profile of nivolumab (NIVO) in patients (pts) with advanced melanoma (MEL): a pooled analysis. *J. Clin. Oncol.* **33**, 9018–9018 (2015).
46. Jiang, Y. et al. Identification and characterization of a novel RF-amide peptide ligand for orphan G-protein-coupled receptor SP9155. *J. Biol. Chem.* **278**, 27652–27657 (2003).

47. Cohen, J. C., Boerwinkle, E., Mosley, T. H. & Hobbs, H. H. Sequence variations in PCSK9, low LDL, and protection against coronary heart disease. *N. Engl. J. Med.* **354**, 1264–1272 (2006).
48. Furie, R. et al. Anifrolumab, an anti-interferon-α receptor monoclonal antibody, in moderate-to-severe systemic lupus erythematosus. *Arthritis Rheumatol.* **69**, 376–386 (2017).
49. Bradford, H. F. et al. Inactive disease in patients with lupus is linked to autoantibodies to type I interferons that normalize blood IFNα and B cell subsets. *Cell Rep. Med.* **4**, 100894 (2023).
50. Bastard, P. et al. Autoantibodies neutralizing type I IFNs are present in ~4% of uninfected individuals over 70 years old and account for ~20% of COVID-19 deaths. *Sci. Immunol.* **6**, eabl4340 (2021).
51. Michot, J. M. et al. Immune-related adverse events with immune checkpoint blockade: a comprehensive review. *Eur. J. Cancer* **54**, 139–148 (2016).

Methods

Ethics oversight

For the Yale cohort, the study was conducted with approval from the Yale University Institutional Review Board (HIC# 0608001773, HIC# 1512016953 and HIC# 1401013290), and written informed consent was obtained from all participants. For the MT cohort, approval was obtained from local Institutional Review Boards and a central Institutional Review Board (Sterling). All patient samples and clinical data elements were de-identified, and all protected health information was removed in accordance with the Health Insurance Portability and Accountability Act.

Patient recruitment

Yale cohort. Patients were approached at Yale New Haven Hospital upon initiating or while receiving treatment with anti-PD1, anti-PDL1, or anti-PD1 combined with anti-CTLA4. They were invited to participate by donating blood and clinical data. All patients with available samples and relevant clinical data were included for REAP processing, without any additional selection bias. For the MT cohort, the MT Group collected samples from multiple sources, including academic centres, community hospitals and private practices. All patients receiving CPIs with available samples and relevant clinical data were included for REAP processing, without any additional selection bias.

Human exoproteome yeast library generation

The yeast library was generated as previously described[3]. An updated version of the library was used in this study (Supplementary Table 5). In brief, 4,511 human membrane and secreted proteins were curated from the UniProt (2018)[52] and SwissProt database (January 2018)[52]. From this curated list, 6,593 extracellular domains, each exceeding 15 amino acids in length, were selected to construct the library. Antigens were PCR amplified using cDNA templates acquired from GE Dharmacon and DNASU. In cases in which the cDNA template for an antigen was unavailable or where PCR amplification failed, the antigens were synthesized by Twist Bioscience. Following this, all sequences were then integrated into a barcoded yeast-display vector and electroporated into yeast. Yeast with positive antigen display, marked by FLAG tag, were sorted out by Sony SH800Z cell sorter. Barcode–antigen pairs were identified using a custom Tn5-based sequence approach. In the final library, 6,172 antigens from 4,306 proteins were confidently detected.

REAP

Antibody purification and yeast depletion. IgG purification was performed as previously described[3]. Of PBS-washed protein G magnetic resin (Lytic Solutions), 20 µl was then mixed with 25 µl inactivated plasma and the mixture was incubated at 4 °C for 3 h with agitation. The resin was then washed with sterile PBS and resuspended in 90 µl of 100 mM glycine (pH 2.7). Following a 5-min incubation at room temperature, the supernatant was separated and mixed with 10 µl of 1 M Tris (pH 8.0). IgG concentration was then determined using a NanoDrop 8000 Spectrophotometer (Thermo Fisher Scientific). Purified IgG was then combined with 10^8 induced yeast cells (with empty pDD003 vector) in 100 µl PBE (PBS with 0.5% BSA and 0.5 mM EDTA). After a 3-h incubation at 4 °C with shaking, the mix was filtered through 96-well 0.45-µm plates (Thomas Scientific) with 3,000*g* for 3 min to collect the yeast-depleted IgG.

Yeast library-antibody selection. The screening was performed as previously described[3]. In brief, the yeast library was grown in SDO-Ura at 30 °C to achieve OD between 5 and 7. The library was then induced in 1:10 SDO-Ura:SGO-Ura at 30 °C with starting OD at 1 for 20 h. Before selection, plasmid DNA was isolated from 400 µl of the induced library (Zymoprep Yeast Cell Plasmid Miniprep II kit) as the baseline reference for antigen frequency. Of yeast-depleted IgG, 10 µg was incubated with 10^8 induced library yeast in 100 µl PBE with shaking for 1 h at 4 °C, followed by 30 min of incubation with 1:100 biotin anti-human IgG Fc antibody (clone HP6017, BioLegend) in 100 µl PBE and 30 min of incubation with 1:20 Streptavidin MicroBeads (Miltenyi Biotec) in 100 µl PBE. Streptavidin MicroBeads-captured yeast were positively selected by Multi-96 Columns (Miltenyi Biotec) placed in a MultiMACS M96 Separator (Miltenyi Biotec). Selected yeast cells were recovered in 1 ml SDO-Ura at 30 °C for 24 h.

NGS library preparation and sequencing. Next-generation sequencing (NGS) was performed as previously described[3]. In brief, DNA was extracted from yeast libraries using Zymoprep-96 Yeast Plasmid Miniprep kits (Zymo Research). Purified plasmids were amplified and indexed (2 rounds of Phusion PCR, 24 cycles per round), pooled, gel purified and sequenced on an Illumina NextSeq550 with 75-bp single-end sequencing. A minimum of 300,000 reads on each sample and 3 million reads for pre-selection library were collected.

Clinical data processing

Response to therapy. Radiographic responses to therapy were assessed using the RECIST criteria. For downstream binary analyses, we categorized patients who experienced a radiographic complete response or partial response as responders, and those with stable disease and progressive disease as non-responders, according to their best response at any point in the administered regimen.

Processing of potential confounding variables. Previous treatment with CPIs and CPI treatment regimen (PD1 alone versus PD1 and CTLA4), Eastern Cooperative Oncology Group (ECOG) performance status and plasma LDH levels were extracted when available from clinical charts. LDH levels were log transformed. When available, tumour PDL1 status was binned into categories based on tumour staining: no expression (tumour staining of less than 1%), low expression (1–50%) and high expression (more than 50%). In downstream analyses, we represented PDL1 status as a categorical variable with missing PDL1 data as a separate level.

To identify variables that might confound the association between AAb reactivity and response to CPI treatment, we assessed univariate associations between age, sex, cancer stage, CPI treatment regiment, previous CPI status, log LDH and ECOG status (Supplementary Table 2), in the full pan-cancer cohort as well as in the NSCLC, melanoma and renal cell carcinoma subcohorts. In downstream AAb-treatment response analyses, we adjusted for variables based on the significance of the univariate association between potential confounders and the response variable, data completeness and potential clinical relevance.

REAP data analysis

REAP score calculation was as previously described[3]. A modified REAP scoring system was used in this study. The aggregate enrichment E_s (log fold change with zeroes in the place of negative fold changes) between the frequency of a protein in a sample and in the pre-selection library was calculated for each protein. Similarly, the aggregate enrichment E_b between the frequency of each protein in blank samples compared with the pre-selection library was also calculated. To account for background enrichment in the absence of sample, we subtracted blank enrichment E_b from sample enrichment E_s. We defined the REAP score as $\max(\log[\exp(E_s) - \exp(E_b)],0)$ when $E_s > E_b$, and 0 otherwise.

AAb-treatment response association analysis. We assessed the association between the presence of each AAb identified in the cohort and the likelihood of patient response to immune checkpoint inhibitor treatment. Here response was categorized as a complete response or a partial response. For each patient, REAP scores from multiple longitudinal samples were consolidated by selecting the maximum REAP score observed across all time points. In instances with multiple replicates

for a given sample, the mean REAP score was computed. To dichotomize the presence or absence of an AAb, REAP scores were binarized. A threshold of REAP = 1 was implemented, where: AAb = 1 indicates REAP ≥ 1 (presence) and AAb = 0 indicates REAP < 1 (absence).

For each AAb, the Firth logistic regression was used to calculate association with treatment response. The model was adjusted for known confounders cancer type, age, previous CPI status, CTLA4 treatment status and PDL1 status, represented as:

Response ~ AAb + age + cancer type + CTLA4 + previous CPI + PDL1

The Firth logistic regression, as opposed to conventional logistic regression, incorporates a penalty to the likelihood using the Jeffreys prior. This modification ameliorates challenges posed by low-frequency AAbs or situations of perfect separation. The regression analysis yielded adjusted odds ratios and associated *P* values, computed using the logistf package in R.

For the cancer-type-specific analyses (Extended Data Fig. 9), we adjusted for different sets of variables depending on data completeness and clinical relevance. The melanoma-specific regressions were adjusted for age, previous CPI treatment, CTLA4 treatment status and log-transformed LDH. The NSCLC-specific regressions were adjusted for age, previous CPI treatment, CTLA4 treatment status and PDL1 status. The renal cell carcinoma regressions were adjusted for age, previous CPI treatment and CTLA4 treatment.

For a more detailed pathway analysis, we utilized the gseapy package in Python[53], which is an implementation of the gene set enrichment analysis algorithm. We ranked each AAb using its odds ratio, then manually categorized these AAbs into broad protein families and known biological pathways. The complete AAb repertoire served as our background reference. Within this context, we evaluated the AAbs in selected categories for their enrichment correlation with treatment outcomes.

AAb discovery rate analysis. We performed a discovery rate analysis to assess the relationship between the number of patients in the cohort and the number of unique antigens with AAb reactivities observed. We took a random permutation of the patients. Beginning with the first patient in this permutation, we successively tallied the cumulative number of unique antigens exhibiting AAb reactivities as we incorporated data from each subsequent patient. For a more granular understanding, we maintained separate cumulative counts based on the frequency of antigen occurrence within the cohort, distinguishing common antigens (defined as antigens with a frequency greater than or equal to 0.01 in the cohort) from rare antigens (antigens with a frequency less than 0.01 in the cohort).

AAb persistence analysis. In the Yale cohort, we identified and tracked REAP hits exhibiting a REAP score greater than 1 on day 0. A REAP hit was defined to persist as long as it maintained a REAP score exceeding 1. The persistence of a REAP hit concluded upon observing the first sample where the REAP score was less than 1 and no subsequent resurgence of the score above this threshold. In instances in which REAP hits were observed in the last longitudinal sample of a patient without subsequent data to confirm persistence or decline, these hits were right censored to account for potential truncation of data. To visually represent the persistence of REAP hits over time and estimate the median persistence duration, we used the Kaplan–Meier survival curve. The curve, along with the median persistence time, was computed using the survival and survminer packages in R.

Lasso machine learning model. A Lasso model was trained to predict sample type (cancer versus healthy). The input for the model was binarized REAP reactivity scores from single samples for 131 healthy participants and 217 pre-treatment patients with cancer. To limit the number of features in the model, we only considered antigens observed in greater than 5% and less than 60% of samples, resulting in 163 features. To assess model performance, we ran sevenfold cross-validation with hyperparameter tuning as part of the training pipeline. The performance of the models on each test fold was visualized using receiver operating characteristic curves.

AAb–irAE association analysis. For a given irAE, patients with side-effect grades above 1 were classified as the positive cohort, and those with grade 0 as the negative cohort. We conducted Fisher's exact tests between two cohorts on genes with a higher occurrence ratio in the positive cohort. The resulting *P* values were corrected for the number of irAEs and transformed using $-\log_{10}$. The final data were visualized in a Manhattan plot by Prism software.

AAb ELISA

Recombinant protein was generated using Expi293F cells (A14527, Thermo Fisher Scientific) according to the manufacturer's instructions. Of recombinant protein antigen, 250 ng in 100 µl PBS was added to wells of 96-well Immuno 2HB plates (Thermo Fisher Scientific). Plates were sealed and placed in 4 °C overnight. After incubation, plates were washed once with 225 µl wash buffer (PBS + 0.05% Tween 20). Of blocking buffer (2% HSA in PBS pH 7.0), 150 µl was added to each well and incubated at room temperature for 2 h. Plates were then washed three times with 225 µl wash buffer. Of plasma dilutions (starting with either 1:50 or 1:100 dilution, in blocking buffer), 100 µl was added to the corresponding wells and incubated at room temperature for 2 h. Plates were subsequently washed six times with 225 µl wash buffer. 1:5,000 HRP anti-human IgG Fc (A00166, GenScript) or isotype-specific antibody (410603, BioLegend; clone HP6001 (IgG1), clone 31-7-4 (IgG2), clone HP6050 (IgG3) and clone HP6025 (IgG4), Southern Biotech) in 100 µl blocking buffer was added to each well and incubated at room temperature for 1 h. Plates were then washed six times with 225 µl wash buffer. Of TMB substrate (BD Biosciences) 1:1 mixture, 50 µl was added to each well and developed at room temperature in the dark for 15 min. Of 2 N/1 M H_2SO_4, 50 µl was added to each well to terminate the TMB reaction. Absorbance at 450 nm and 570 nm was measured in a Synergy HTX Multi-Mode Microplate Reader (BioTek).

AAb functional validation

Cell signalling assessment of anti-OSM AAbs. TF-1 cells (CRL-2003, American Type Culture Collection; cultured in RPMI + 10% FBS + 2 ng ml^{-1} recombinant hGM-CSF + 1 mM sodium pyruvate) were used to assess STAT3 phosphorylation (pSTAT3) downstream of OSM. For the experiment, IgG was purified from plasma as described above and normalized to 2 mg ml^{-1}. TF-1 cells were starved of hGM-CSF 18 h before the experiment. OSM (495-MO, R&D Systems) was pre-incubated with 20 µg of purified IgG from different samples at room temperature for 30 min. Then, OSM and antibody mixture were added to the starved TF-1 cells (in the 96-well plate with 400,000 cells per well) in a final volume of 100 µl (final concentration for OSM was 0.65 ng ml^{-1}). Following a 15-min incubation, the cells were pelleted and fixed in 4% paraformaldehyde for 20 min. Cells were then washed with PBS two times and permeabilized with pre-cold 100% methanol on ice for 45 min. Cells were then washed with PBE two times, followed by staining with 1:50 PE anti-pSTAT3 (612569, BD) and 1:100 human TruStain FcX (422302, BioLegend) at room temperature for 1 h. Cells were then washed with PBE two times and acquired on a flow cytometer (SA3800, Sony) to record MFI in the PE channel.

Cell signalling assessment of anti-IL-6 AAbs. THP-1 cells (TIB-202, American Type Culture Collection; cultured in RPMI + 10% FBS) were used to assess pSTAT3 signalling downstream of IL-6. IL-6 (206-IL, R&D Systems) was pre-incubated with 2 µl plasma from different samples at room temperature for 30 min. Then, IL-6 and plasma mixture were

added to the THP-1 cells (in the 96-well plate with 400,000 cells per well) in a final volume of 100 µl (final concentration for IL-6 was 260 ng ml^{-1}). After a 15-min incubation, the cells were processed as the method described above in the section 'Cell signalling assessment of anti-OSM AAbs'.

Cell signalling assessment of anti-IFNα AAbs. THP-1 cells were used for validation. IFNα2a (CYT-204, ProSpec), IFNα4 (10336-H08B, Sino Biological) or IFNα8 (11018-IF-010, R&D Systems) was pre-incubated with 2 µl plasma from different samples at room temperature for 30 min. Then, IFNα and plasma mixture were added to the THP-1 cells (in the 96-well plate with 400,000 cells per well) in a final volume of 100 µl (final concentration for IFNα2 was 0.8 ng ml^{-1} and for IFNα4 was 1.8 ng ml^{-1}). After a 15-min incubation, the cells were processed as the method described above in the section 'Cell signalling assessment of anti-OSM AAbs', but with PE anti-pSTAT1 (612564, BD) substituted for anti-pSTAT3.

TF-1 cell viability-based validation of anti-TL1A AAbs. TL1A has previously been reported to induce apoptosis in TF-1 cells[54]. IgG was purified from plasma using protein G and was normalized to 2 mg ml^{-1}. Ten thousand TF-1 cells were seeded in each well and treated with 10 µg ml^{-1} of cycloheximide (C7698, Sigma-Aldrich) and 20 ng ml^{-1} of TL1A (1319-TL, R&D Systems). Concurrently, 20 µg of purified IgG from different samples was added to the corresponding wells. Following a 24-h incubation at 37 °C in a 5% CO_2 humidified incubator, 10 µl Resazurin (AR002, R&D Systems) was added to each well. After an additional 24-h incubation, fluorescence was measured using a Synergy HTX Multi-Mode Microplate Reader (BioTek), with an excitation wavelength of 544 nm and an emission wavelength of 590 nm.

BMPR1A–BMPR2 dimerization assay for anti-BMPR1A/BMPR2 AAb validation. The Eurofins DiscoverX PathHunter eXpress BMPR1A–BMPR2 Dimerization Assay kit (931006E3CP0M, Eurofins DiscoverX) was used for validation according to the manufacturer's protocol. Cells were thawed and seeded in 100 µl of supplied culture media in 96-well plates. Twenty-four hours later, 2 µl of plasma samples were added to the corresponding wells and incubated for 1 h. Then, recombinant BMP2 (120-02C, PeproTech) was added to each well to a final concentration of 200 pM. After 6 h of stimulation, the assay buffer was added to each well. One hour later, the absorbance was measured using a Synergy HTX Multi-Mode Microplate Reader (BioTek) at a wavelength of 528/20 nm.

PBMC immunophenotyping in patients with cancer

PBMC immunophenotyping was performed as previously described[55]. In brief, frozen PBMCs from patients were thawed in RMPI + 10% FBS medium in the presence of Benzonase (E8263-25KU, Sigma-Aldrich) and washed with PBS buffer twice before staining. The LIVE/DEAD Fixable Blue Dead Cell Stain Kit (L23105, Invitrogen) was used to identify dead cells, with staining conducted at room temperature for 15 min. Subsequently, an Fc receptor blocker (564220, BD) was introduced to prevent nonspecific binding. For surface staining, the cell suspension was incubated with a mixture of antibodies at 4 °C for 30 min. The antibodies included anti-human CD3 (UCHT1), CD4 (OKT4), CD8 (SK1), CD14 (63D3), CD16 (3G8), CD19 (SJ25C1), CD56 (NCAM16.2), CD28 (CD28.2), CD45 (2D1), CD27 (O323), CD123 (6H6), CD11c (3.9), IgD (IA6-2), IgM (MHM-88), IgG (G18-145), CXCR5 (RF8B2), CD141 (1A4), CD1c (L161), LAIR1 (REA447), Siglec-1 (7-239) and CD163 (GHI/61). Following this, the cells were permeabilized and fixed at 4 °C for 1 h using the eBioscience Foxp3/Transcription Factor Staining Set (00-5523-00, Invitrogen). Intracellular staining was carried out at 4 °C for 1 h with the addition of anti-human CD68 (Y1/82A). Cells were acquired on a spectral cytometer (Cytek Aurora) and data were analysed by FlowJo (v10).

Mouse housing conditions and ethics oversight

Eight-to-ten-week-old C57BL/6 and BALB/c mice were purchased from Charles River Laboratories. Mice were housed in groups of five to six per cage and maintained under specific-pathogen-free conditions on a 12-h light–dark cycle (lights on at 7:00), at a temperature of 22–25 °C and relative humidity of 30–70%. All mice had ad libitum access to regular rodent chow and sterilized water. All procedures used in this study complied with federal guidelines and the institutional policies of the Yale School of Medicine Animal Care and Use Committee.

Mouse tumour treatment studies

MC38b, B16-F10 and CT26 cells were cultured in RPMI + 10% FBS. Eight-to-ten-week-old age-matched C57BL/6 female mice were used for the MC38b and B16-F10 tumour models and 8–10-week-old age-matched BALB/c female mice were used for the CT26 tumour model. Five hundred thousand tumour cells (resuspended in 100 µl DPBS) were subcutaneously injected into the flank region of mice at day 0. At day 8, mice with tumours less than 50 mm^3 or greater than 150 mm^3 were excluded. Remaining mice were randomized into designated groups to ensure an approximately equal average weight and tumour size. Mice were then treated with the designated test drugs by intraperitoneal injection every 3 days for a total of five doses. The drugs were diluted in sterile DPBS and dosed as follows: anti-mouse PD1 (RMP1-14, Bio X Cell) at 200 µg per dosage, anti-mouse CTLA-4 (9H10, Bio X Cell) at 100 µg per dosage, anti-mouse IFNAR1 (MAR1-5A3, Bio X Cell) at 1 mg per dosage, anti-mouse IFNα (TIF-3C5, Ichorbio) at 500 µg per dosage and anti-mouse TL1A (5G4.6, Bio X Cell) at 200 µg per dosage. Control groups were treated with sterile DPBS. Mice weight and tumour growth were tracked twice per week. Tumour volume was calculated using volume = 0.5 × length × width × width. Mice were euthanized when tumours reached end points (volume greater than or equal to 1,000 mm^3 for the MC38b and CT26 models and 1,500 mm^3 for the B16-F10 model). Mice demonstrating complete tumour clearance were maintained until day 60.

Mouse tumour tissue processing

Tumours were dissociated for analysis as previously described[56]. In brief, digestion media (RPMI-1640 supplemented with 1% FBS, 1 mg ml^{-1} collagenase IV (17104019, Thermo Fisher Scientific) and 0.2 mg ml^{-1} DNase I (10104159001, Sigma-Aldrich)) were pre-warmed in 37 °C. Tumour tissues were minced and incubated in digestion media for 20 min at 37 °C with shaking. Then, R10 media (RPMI-1640 with 10% FBS) were added to neutralize protease activity and tumour tissues were smashed through 70-µM cell strainers to prepare single-cell suspensions. Cells were then washed twice with R10 media. ACK buffer (A1049201, Thermo Fisher Scientific) was then used for red blood cell lysis, followed by wash two times with R10 media. In final, cells were resuspended in 1 ml R10 media for downstream staining. Cell concentration was determined using a CellDrop Automated Cell Counter (DeNovix).

Cytokine secretion assay of tumour-infiltrating lymphocytes

Mice with CT26 tumours were engrafted and treated in the same way as for the tumour growth studies. Mice were euthanized 24 h after the second treatment dose at the indicated time point, and tumors were harvested for analysis as described above. For ex vivo cytokine secretion, single-cell suspensions of processed tumour tissue were stimulated with a PMA–Ionomycin cocktail (1:500; 423304, BioLegend) for 30 min at 37 °C, and Golgi Stop/Plug (1:1,000; 554724/555029, BD) was added for an additional incubation for 4 h at 37 °C. Cell cultured in media alone (without stimulation) was used as a negative control. All samples were stained with LIVE/DEAD Fixable Blue Kit to identify dead cells and incubated with Fc receptor blocking antibody (101320, BioLegend). Cell-surface staining of single-cell suspensions from tumours

was performed using fluorophore-conjugated antibodies: anti-CD3 (17A2), CD4 (GK1.5), CD8a (53-6.7), CD49b (DX5), PD1 (RMP1-30) and TIM3 (RMT3-23). Cell suspensions were fixed and permeabilized using the Cytofix/Cytoperm kit (554714, BD Biosciences) followed by intracellular staining: anti-IFNγ (XMG1.2), IL-10 (JES5-16E3), perforin (S16009A), TNF (MP6-XT22), Ki67 (16A8) and granzyme B (QA16A02). Cells were acquired on a spectral cytometer (Cytek Aurora) and analysed by FlowJo (v10).

TL1A and DR3 expression analysis

Mice bearing MC38b tumours were euthanized 7 days after tumour engraftment. Tumors were dissociated for analysis as described above. Single-cell suspensions of processed tumour tissue were stained with the LIVE/DEAD Fixable Blue Kit to identify dead cells and incubated with Fc receptor blocking antibody (101320, BioLegend). Cell-surface staining of single-cell suspensions from tumours was performed using fluorophore-conjugated antibodies: anti-CD45 (30-F11), CD3 (17A2), CD4 (GK1.5), CD8a (53-6.7), CD49b (DX5), CD11b (M1/70), NK1.1 (PK136), B220 (RA3-6B2) and DR3 (4C12). Then, cell suspensions were fixed and permeabilized using the Cytofix/Cytoperm kit (554714, BD Biosciences) followed by intracellular staining: anti-TL1A (Tandys1a). Cells were acquired on a spectral cytometer (Cytek Aurora) and analysed by FlowJo (v10).

Assessment of tumour-infiltrating lymphocyte apoptosis

Tumours were dissociated for analysis as described above. Mice engrafted with MC38b tumours from the anti-PD1-treated group were euthanized, and 500,000 cells from tumour digests were seeded into 96-well plate for each well in 200 µl culture media (RPMI-1640 supplemented with 10% FBS, 10 mM HEPES, 1% penicillin and streptomycin, 50 µM β-mercaptoethanol, 100 IU ml^{-1} mouse IL-2 (575404, BioLegend) and 5×10^5 anti-mouse CD3/CD28 beads (11456D, Fisher Scientific)). Of anti-mouse TL1A (5G4.6, Bio X Cell) antibody, 2 µg was added to the corresponding wells and DPBS was used for negative controls. After 48 h of incubation, cells were collected and analysed for apoptosis by flow cytometry as described above. All samples were stained with the LIVE/DEAD Fixable Blue Kit (L34962, Thermo Scientific) to identify dead cells and incubated with Fc receptor blocking antibody (101320, BioLegend). Cell-surface staining was then performed using fluorophore-conjugated antibodies: anti-mouse CD45 (30-F11), anti-mouse CD3 (17A2), anti-mouse CD4 (GK1.5) and anti-mouse CD8a (53-6.7). After surface staining, cell suspensions were fixed and permeabilized with the Cytofix/Cytoperm kit (554714, BD Biosciences) followed by intracellular anti-Caspase3 (C92 605) staining. Cells were acquired on a spectral cytometer (Cytek Aurora) and data were analysed by FlowJo (v10).

Single-cell RNA sequencing sample preparation

Single-cell RNA sequencing sample preparation was performed as previously described[56]. In brief, mice used for single-cell RNA sequencing were engrafted with MC38b and treated with anti-mouse PD1 and anti-mouse TL1A the same way as for the tumour growth studies. Mice were euthanized 24 h after the second dose of saline, anti-mouse PD1 and/ or anti-mouse TL1A, and tumors were harvested for analysis. Tumour tissues were processed as aforementioned. Cell-surface staining of single-cell suspensions from tumours was performed after wash two times with FACS buffer (PBS supplemented with 2% FBS). All samples were first stained with LIVE/DEAD Fixable Blue to exclude dead cells and incubated with Fc receptor blocking antibody (101320, BioLegend). Then, cells were stained with anti-CD45 (30-F11) and anti-CD3 (17A2). Biological replicates for saline control ($n = 2$) and the treated group ($n = 4$) were individually processed. Biological replicates were then pooled together at the single-cell suspension stage before sorting with equivalent number of cells from each replicate. The following populations were sorted: for P1, $CD45^+CD3^+$ (tumour-infiltrating lymphocytes); for P2, $CD45^+CD3^-$ (non-tumour-infiltrating lymphocyte immune cells); and for P3, $CD45^-CD3^-$ (tumour and stromal cells). P1, P2 and P3 for each sample were then mixed back together at a 9:9:2 ratio, respectively. Twenty thousand cells from each treatment condition were loaded onto the 10X Genomics Chromium System. Library preparation was performed with 10X Genomics reagents according to the manufacturer's instructions by the Yale Center for Genome Analysis. Libraries were then sequenced with an Illumina NovaSeq 6000 at the Yale Center for Genome Analysis.

Single-cell RNA sequencing data analysis

The Scprep and Scanpy packages in Python were used to process the matrix and perform downstream analysis according to their documentations. The matrix was preprocessed by excluding cells with fewer than 200 detected reads, selecting only those within the 10–90th percentiles of total gene expression, and removing cells in the top 10% of mitochondrial gene expression. Genes detected in less than three cells were also excluded. Expression values were then log normalized with a scaling factor of 10^4. The preprocessed matrix was then dimensional reduced by principal component analysis and the first 50 components were used by tSNE analysis to visualize the data. The Phenograph package was used for cell clustering with 'leiden' as clustering algorithm. Clusters containing the following markers were assigned to the corresponding cell types based on the ImmGen datasets for further analysis: T cells (Cd3g), CD8 T cells (Cd8a), CD4 T cells (Cd4), B cells (Ms4a1), myeloid cells (Cd68), natural killer cells (Ncr1) and neutrophils (Lcn2). Cells of interest selected by the cluster and marker were re-processed by principal component analysis, tSNE and Phenograph analysis as described above. For CD8 T cell analysis, the research by Giles et al.[38] (Gene Expression Omnibus: GSE199563) was used as a direct reference for cell subtype assignments. The expression value was scaled for each gene and cluster frequencies for each treatment group were normalized to the total number of cells in each library.

Statistics and reproducibility

Statistical analyses were conducted using R (v4.2.3) and GraphPad Prism (v10.0.0) and are described in the figure legends and Methods. No statistical methods were used to predetermine sample size. The REAP assay was performed in duplicate with two technical replicates for all samples. All in vitro ELISA and signalling assays were conducted in duplicate with two technical replicates. The number of repetitions for other experiments is provided in the figure legends.

Reporting summary

Further information on research design is available in the Nature Portfolio Reporting Summary linked to this article.

Data availability

All data used to generate figures and tables in this study are included in the Source Data. The single-cell RNA sequencing data generated from this study have been deposited in the Gene Expression Omnibus under the accession number GSE294482. The reference dataset used in Extended Data Fig. 8 is under the Gene Expression Omnibus accession number GSE199563. REAP data will be made available on reasonable request from the corresponding authors, subject to restrictions related to patient privacy in accordance with institutional policies and the Health Insurance Portability and Accountability Act. Source data are provided with this paper.

Code availability

The custom code for the analysis of REAP data is available on GitHub (https://github.com/RinglabCancerREAP/Cancer_REAP).

52. The UniProt Consortium. UniProt: the universal protein knowledgebase. *Nucleic Acids Res.* **46**, 2699 (2018).
53. Subramanian, A. et al. Gene set enrichment analysis: a knowledge-based approach for interpreting genome-wide expression profiles. *Proc. Natl Acad. Sci. USA* **102**, 15545–15550 (2005).
54. Migone, T. S. et al. TL1A is a TNF-like ligand for DR3 and TR6/DcR3 and functions as a T cell costimulator. *Immunity* **16**, 479–492 (2002).
55. Qin, K. et al. Exposure of progressive immune dysfunction by SARS-CoV-2 mRNA vaccination in patients with chronic lymphocytic leukemia: a prospective cohort study. *PLoS Med.* **20**, e1004157 (2023).
56. Zhou, T. et al. IL-18BP is a secreted immune checkpoint and barrier to IL-18 immunotherapy. *Nature* **583**, 609–614 (2020).

Acknowledgements We thank all members of the Ring and Kluger laboratories for technical assistance and helpful discussions. Extended Data Fig. 1 was created with Cognition Studio. Figures 1a, 2a, 3b,c,e and 4i and Extended Data Figs. 5a and 6a were created with BioRender (https://biorender.com). Y.D. was supported by a Yale Gruber Fellowship. J.R.J. was supported by the Yale Medical Scientist Training Program. A.M.R. was supported by grants from the Mark Foundation for Cancer Research and the Pew Charitable Trusts, and gifts from the Anderson and Bezos Families. K.C.H. and H.M.K. were supported by grants from the US National Institutes of Health.

Author contributions Y.D., M.A., H.M.K. and A.M.R. designed the study. Y.D. and E.Y.W. established the REAP platform. Y.D. performed the REAP screens. K.C.H., H.M.K. and S.M.C. provided the clinical resources. L.A., M.A. and L.Z. collected the clinical samples, reviewed electronic health records and curated the clinical metadata. Y.D., J.C., H.v.A., Y.K. and L.F. performed the data analysis and data visualization. Y.D., K.Q., J.R.J. and S.F. performed the in vitro and in vivo validation experiments. H.M.K. and A.M.R. supervised the study. Y.D. and A.M.R. wrote the paper with input from all authors.

Competing interests A.M.R., E.Y.W. and Y.D. are inventors of a patent application assigned to Yale University describing the REAP technology (patent number: WO2021189053A1). In addition, A.M.R. is the founder and a director of Seranova Bio, the commercial licensee of REAP. S.M.C. and L.F. are employees of Seranova Bio. H.v.A. holds equity in Seranova Bio. L.A., K.Q., M.A., J.R.J., J.C., L.Z., S.F., Y.K., K.C.H. and H.M.K. declare no competing interests.

Additional information

Supplementary information The online version contains supplementary material available at https://doi.org/10.1038/s41586-025-09188-4.

Correspondence and requests for materials should be addressed to Leon Furchtgott, Harriet M. Kluger or Aaron M. Ring.

Peer review information *Nature* thanks the anonymous reviewers for their contribution to the peer review of this work.

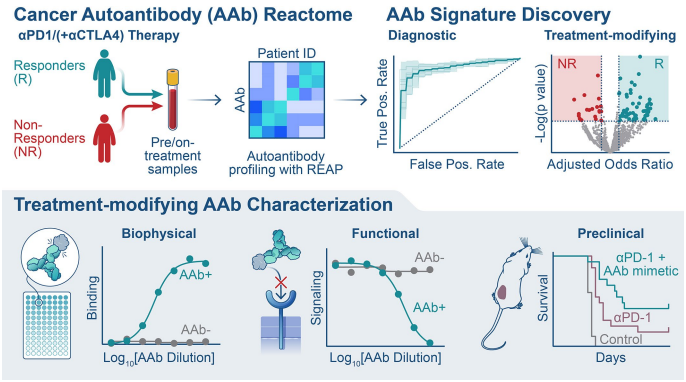

Extended Data Fig. 1 | Graphical abstract. Plasma samples from CPI-treated patients and healthy donors were evaluated for autoantibodies against 6,172 distinct human extracellular antigens using REAP. REAP-derived autoantibody signatures were capable of distinguishing patients from healthy individuals and predicting response to CPI therapy. The impact of individual autoantibodies on clinical outcomes was assessed through calculation of odds ratios, highlighting treatment-enhancing and treatment-inhibiting autoantibodies. Autoantibodies of interest were biophysically validated and assessed for functional activity via ex vivo assays and preclinical models. The graphical abstract was created using Cognition Studio.

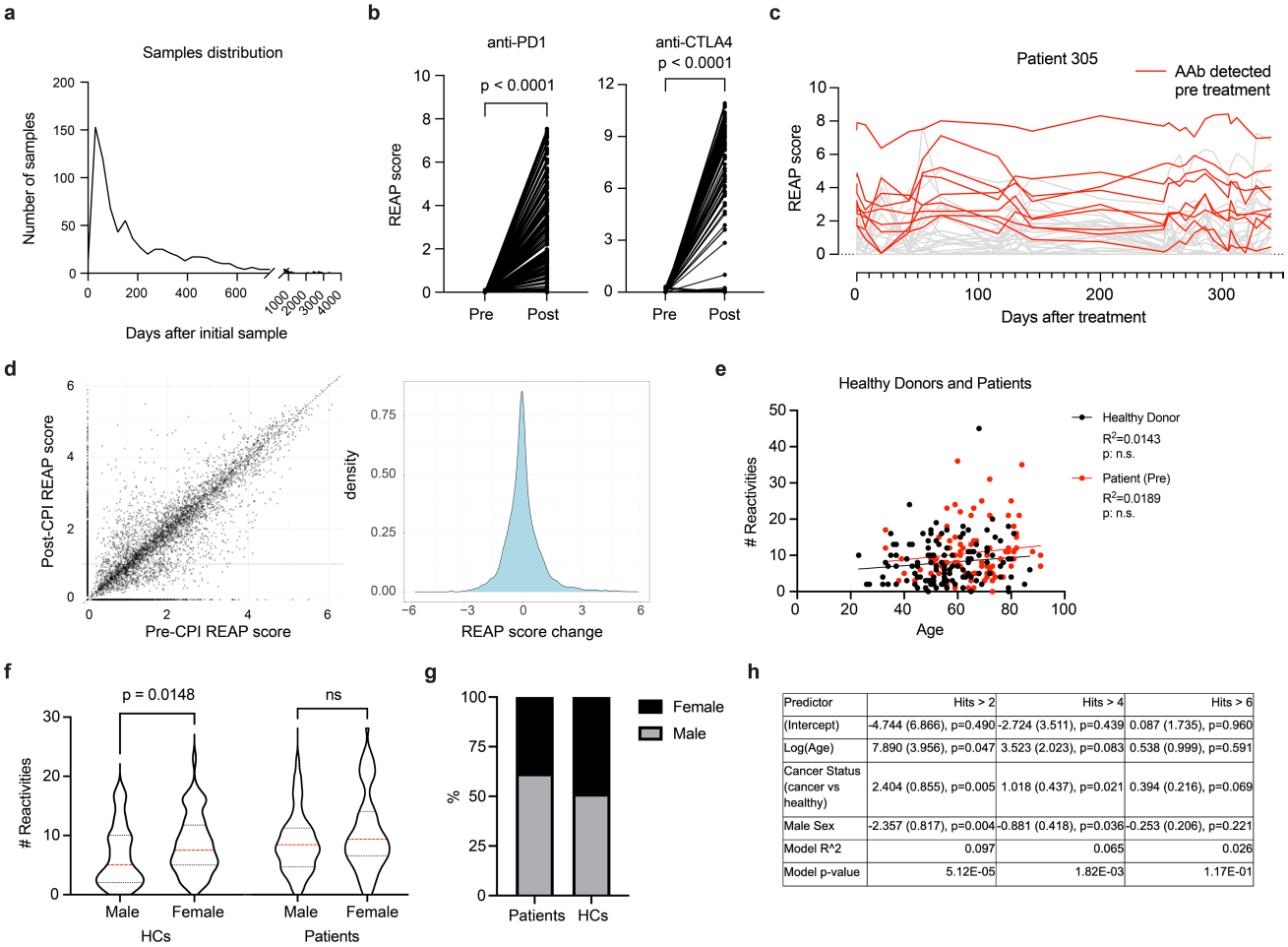

h

Predictor	Hits > 2	Hits > 4	Hits > 6
(Intercept)	-4.744 (6.866), p=0.490	-2.724 (3.511), p=0.439	0.087 (1.735), p=0.960
Log(Age)	7.890 (3.956), p=0.047	3.523 (2.023), p=0.083	0.538 (0.999), p=0.591
Cancer Status (cancer vs healthy)	2.404 (0.855), p=0.005	1.018 (0.437), p=0.021	0.394 (0.216), p=0.069
Male Sex	-2.357 (0.817), p=0.004	-0.881 (0.418), p=0.036	-0.253 (0.206), p=0.221
Model R^2	0.097	0.065	0.026
Model p-value	5.12E-05	1.82E-03	1.17E-01

Extended Data Fig. 2 | Autoantibody dynamics and associations with age and sex. Related to Fig. 1. (**a**) Distribution of longitudinal sample collection over time. (**b**) REAP scores of PD-1 and CTLA4 from pre and post treatment plasma samples. PD−1 signal (n = 189, p = 1.51E-38). CTLA4 signal (n = 212, p = 3.58E-22). Significance was assessed by a paired two-sided Student's t-test. (**c**) Overlay of distinct autoantibody reactivities from an individual patient. Red lines represent autoantibodies detected in the pre-treatment sample and grey lines represent autoantibodies detected post-treatment. (**d**) Scatter plot: Autoantibody REAP values in pre- and post-treatment. Each point represents a detected autoantibody. Density plot: post/pre REAP score differences for all detected reactivities. (**e**) For both healthy donors (controls) and cancer patients, there was a lack of correlation between age and the number of autoantibodies present, as assessed by a linear regression model (p = not significant). (**f**) Comparison of autoantibody numbers between males and females in both healthy donors and cancer patients (pre-treatment). Significance was assessed by a paired two-sided Student's t-test. (**g**) Gender composition of healthy donors and cancer patients. (h) Linear regression models of autoantibody reactivity. Table shows coefficient estimates (standard errors) and p-values for three linear regression models predicting the number of autoantibody hits at different reactivity thresholds (>2, >4, and >6). Cancer Status coefficient represents the difference in number of autoantibodies between pre-treatment cancer patients and healthy controls adjusting for sex and log-transformed age.

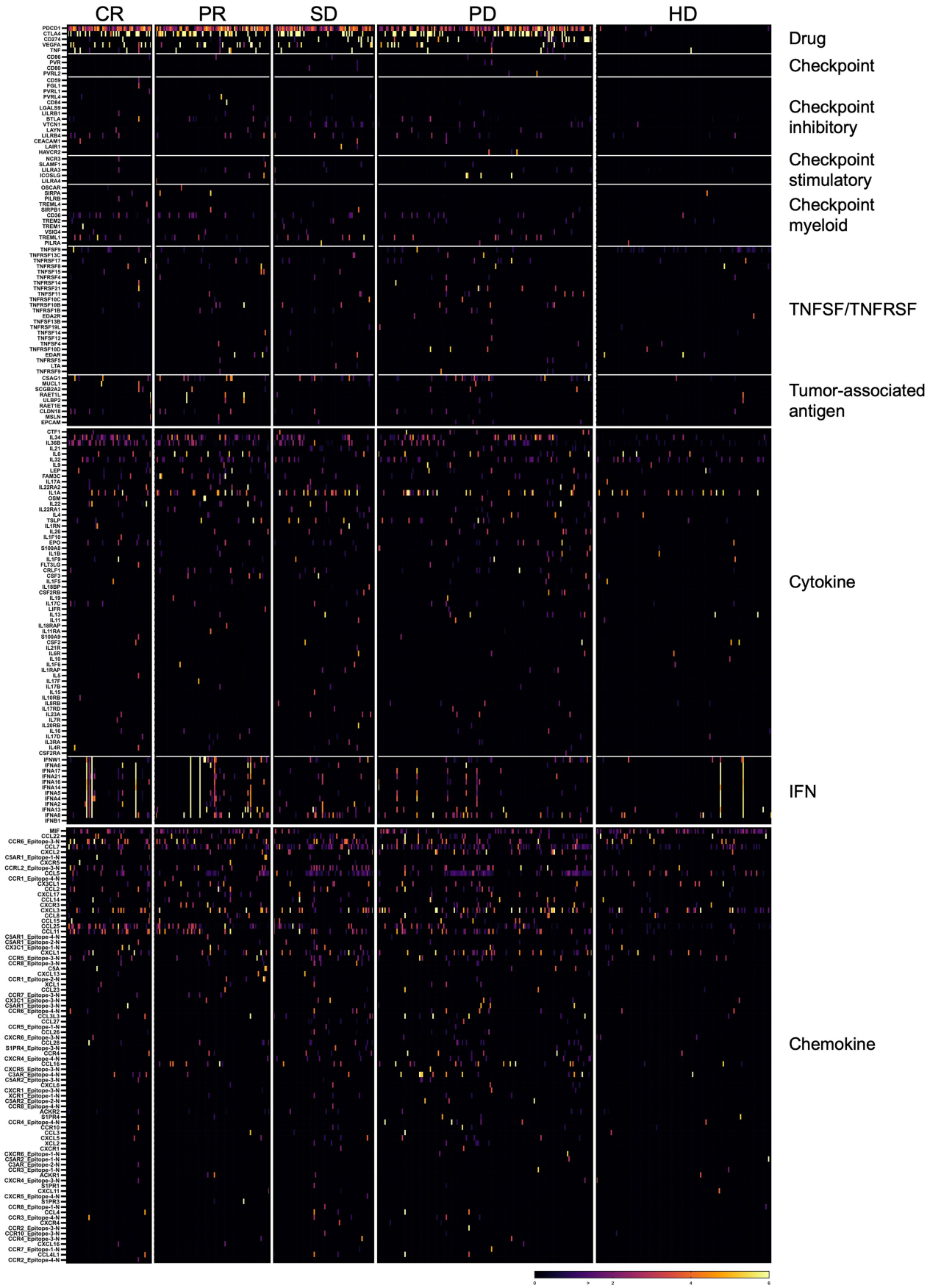

Extended Data Fig. 3 | Heatmap of REAP scores for immune-related proteins. Immune-related proteins were categorized into specific groups as indicated in the figure and patients stratified according to response status.

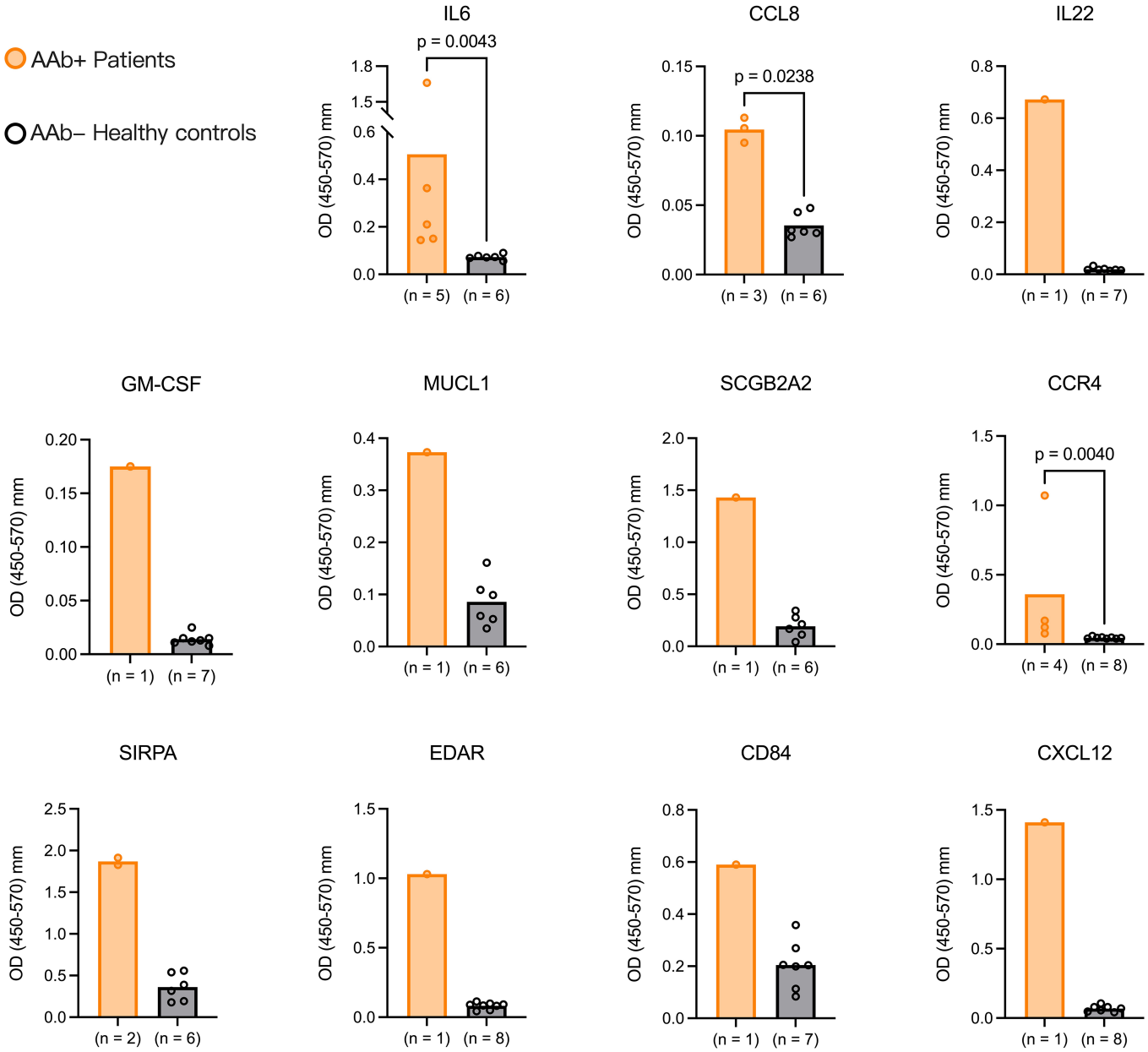

Extended Data Fig. 4 | ELISA validation. ELISA validations for 11 additional REAP-detected autoantigens. The experiments were conducted in unicate with two technical replicates per sample. Data are presented as mean value with dot plots. Significance was assessed by a two-sided Student's t-test.

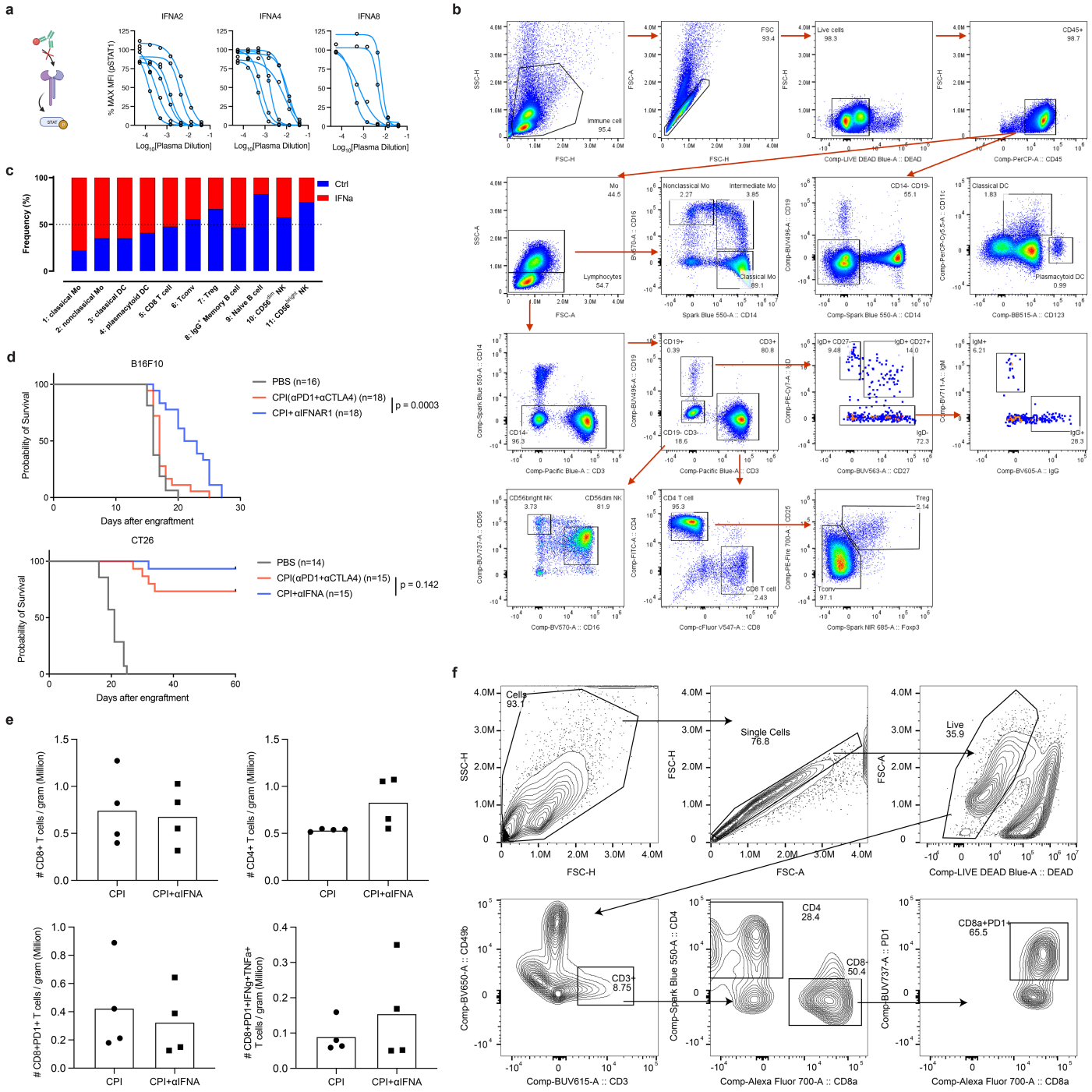

Extended Data Fig. 5 | Additional characterization of plasma and PBMC from patients with neutralizing autoantibodies against IFN-I. (**a**) IFN-I signaling (STAT1 phosphorylation measured by flow cytometry) was assessed across a range of plasma dilutions for the six patients with broadly-reactive IFN-I autoantibodies for IFNA2, IFNA4, and IFNA8 as described in the Methods. Experiment was conducted in duplicate with two technical replicates. The schematic was created using BioRender (https://biorender.com). (**b**) Related to Fig. 3c,d. Flow cytometry gating strategies for monocytes, dendritic cells, B cells, natural killer cells, regulatory T cells, non-regulatory CD4 T cells and CD8 T cells. Antibodies used for staining were listed in the methods. (**c**) Percentage of cells in each cluster for IFN-I autoantibody positive patients compared to control patients. (**d**) Related to Fig. 3f,g. Kaplan–Meier survival curves for mice bearing B16F10 (top) or CT26 (bottom) tumors under different treatment conditions. Figures reflect pooled results from two independent experiments with numbers of animals per group indicated in the legend. Significance was assessed by the log-rank test. (**e**) Related to Fig. 3h,i. Tumor weight-normalized analyses of T cell subpopulations in different treatment groups. Data points are representative of individual tumors measured in unicate. Significance was assessed using a two-sided Student's t-test. (**f**) Related to Fig. 3h,i. Flow cytometry gating strategies for $CD8^+PD1^+$ T cells. Antibodies used for staining were listed in the methods.

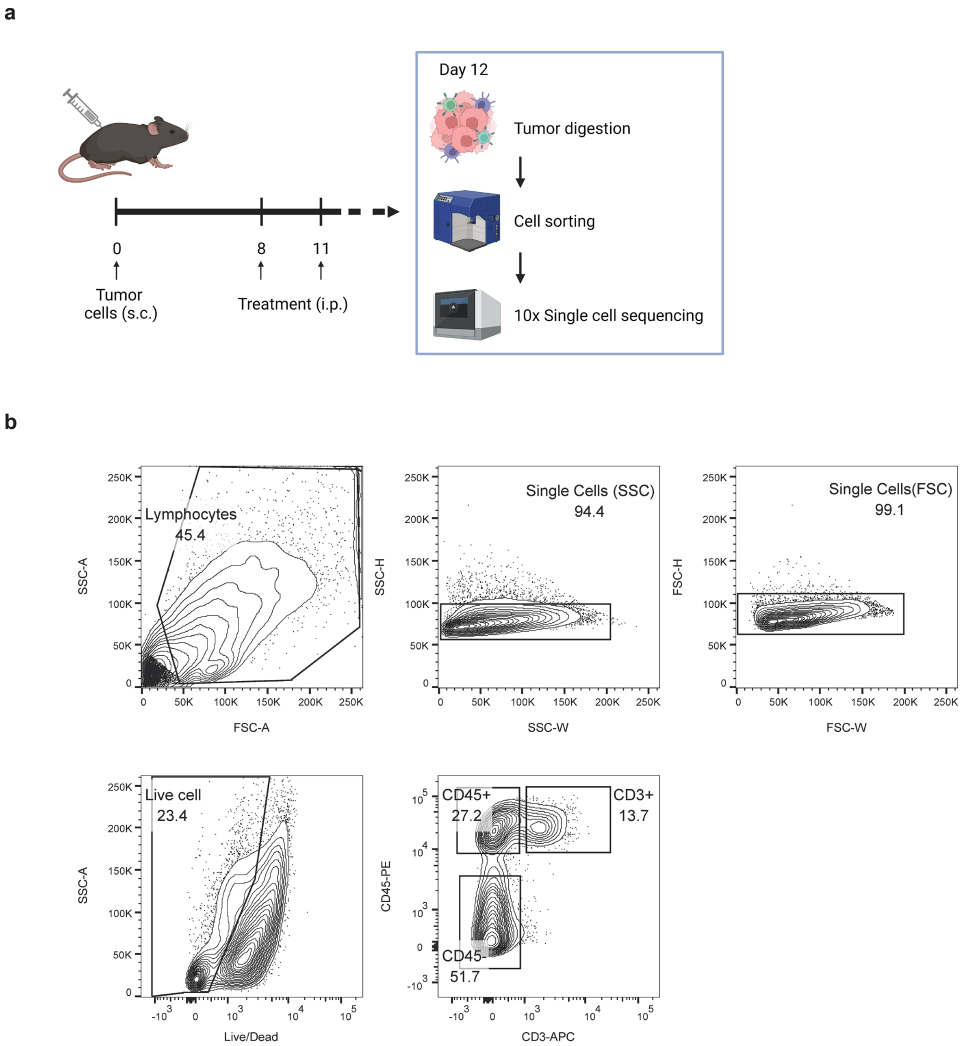

Extended Data Fig. 6 | Single-cell RNA sequencing sample preparation. (**a**) Study design: Mice grafted with MC38b were treated with either anti-mouse PD-1 alone or in combination with anti-mouse TL1A. The mice were euthanized 24 h following the second dose. Tumors were then harvested, digested into a single-cell suspension, sorted into targeted populations, and analyzed using 10x single-cell sequencing. The schematic was created using BioRender (https://biorender.com). (**b**) Flow cytometry gating strategies for sorting out $CD45^+CD3^+$ (TIL cells), $CD45^+CD3^-$ (non-TIL immune cells), and $CD45^-CD3^-$ (tumor and stromal cells).

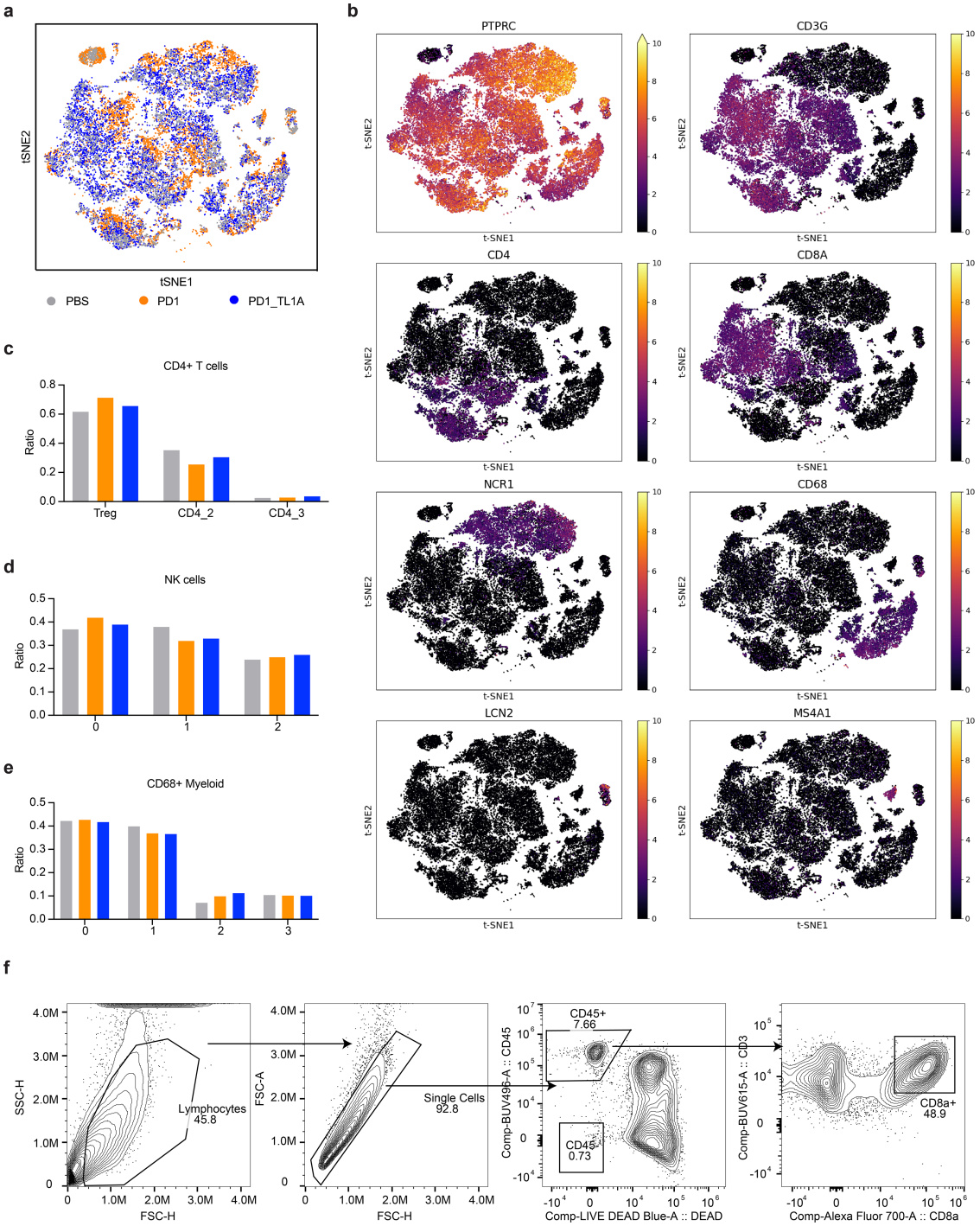

Extended Data Fig. 7 | Single-cell transcriptomic landscape of the TME in anti-PD1 and anti-TL1A treated tumors. (**a**) t-SNE projection showing distribution of all cells colored by treatment condition (dark grey, PBS; orange, anti-PD1; blue, anti-PD1 and anti-TL1A). (**b**) t-SNE plot of all cells colored by expression of genes supporting cell-type assignments. (**c, d, e**) Bar plot showing frequency of CD4 T cells (**c**), NK cells (**d**), and myeloid cells (**e**) within clusters of interests in different treatment group. (**f**) Related to Fig. 4j,k. Flow cytometry gating strategies for CD8 T cells. Antibodies used for staining were listed in the methods.

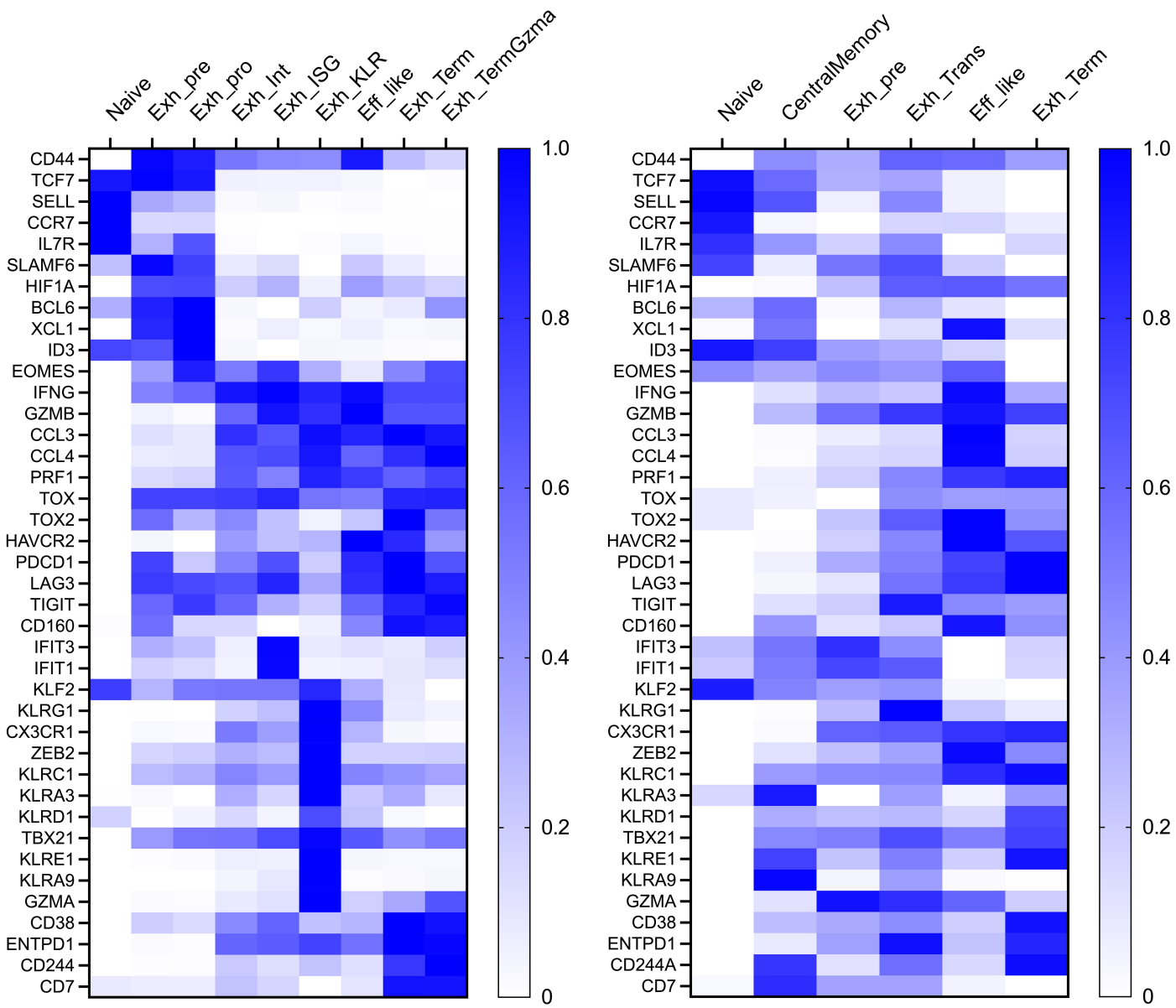

Extended Data Fig. 8 | CD8 T cells subclusters assignment strategy. Giles et al. study[38] on $CD8^+$ T cells subtypes in chronic LCMV infection model was used as a reference to assign cell types in this study. Based on the gene expression pattern, Exh_Int, Exh_ISG and Exh_KLR are grouped as transitory exhausted T cell (Exh_Trans).

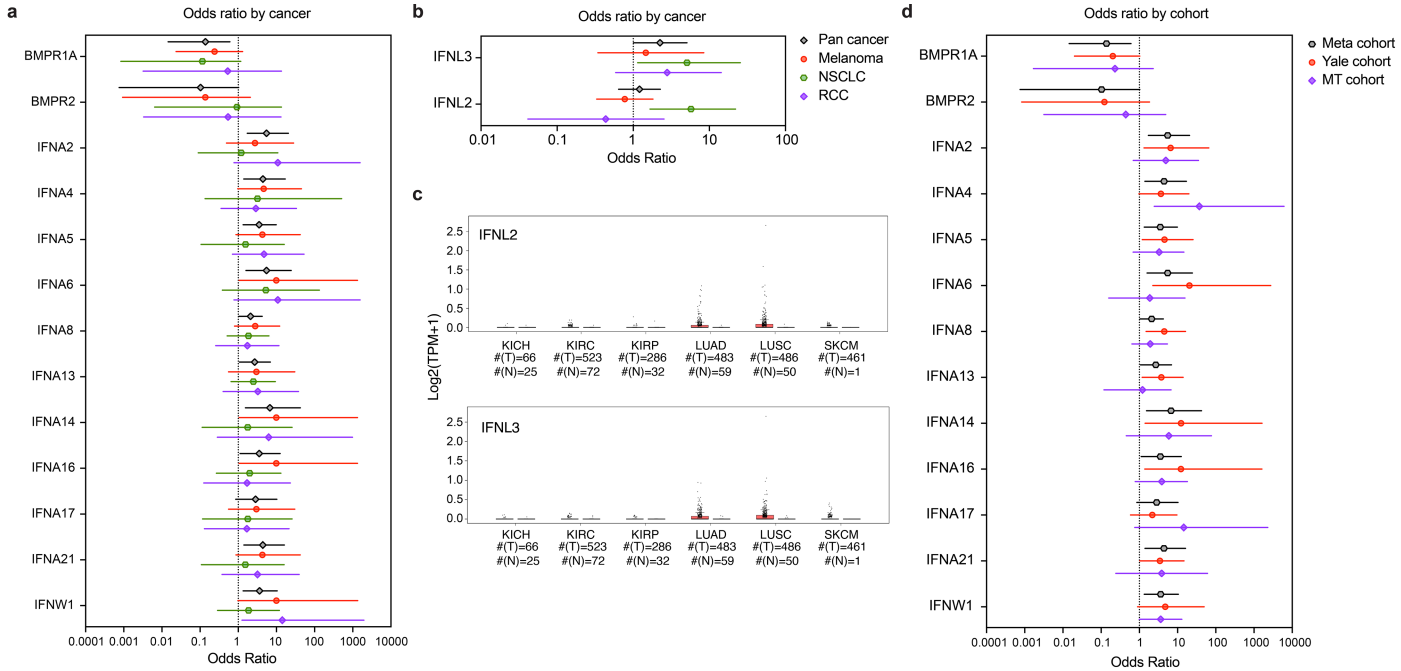

Extended Data Fig. 9 | Comparison of odds ratios for autoantibodies by cancer type and cohort group. (**a, b**) Comparison of odds ratios for anti-IFN-I, anti-IFN-III, and anti-BMPR1A/BMPR2 across different cancer types. Pan cancer (n = 374), melanoma (n = 148), NSCLC (n = 102), RCC (n = 58). Data are presented as odds ratio with 95% confidence intervals. (**c**) Analysis of TCGA transcript expression data for type-III IFN in multiple cancer types. Data are presented as mean value with dot plots. (**d**) Comparison of odds ratios for anti-IFN-I, and anti-BMPR1A/BMPR2 across different cohorts. Meta cohort (n = 374), Yale cohort (n = 249), MT cohort (n = 125). Data are presented as odds ratio with 95% confidence intervals.

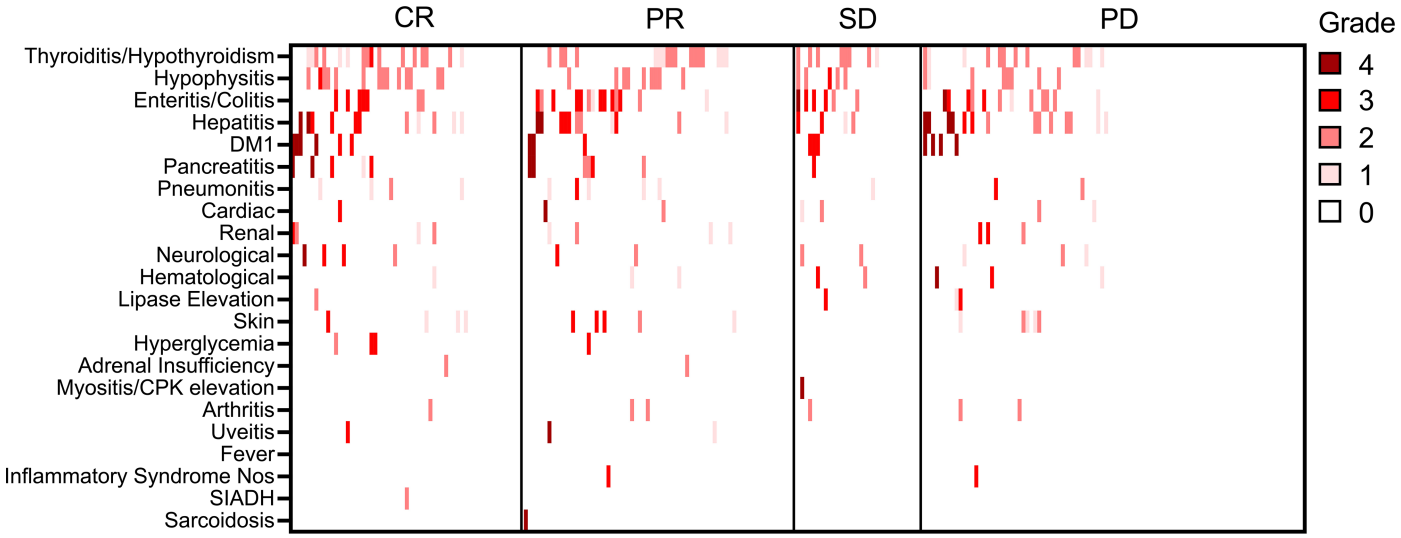

Extended Data Fig. 10 | Composition of irAEs across CPI response status. Related to Fig. 5. This heatmap visualizes the category and severity of irAEs observed. Patients were grouped according to their CPI response status. Color indicates the severity of the specified irAE. Thyroiditis/hypothyroidism, hypophysitis, enteritis/colitis, pancreatitis, and hepatitis were the major observed irAEs in the cohort.

nature portfolio

Corresponding author(s): Leon Furchtgott, Harriet M. Kluger, Aaron M. Ring

Last updated by author(s): Apr 10, 2025

Reporting Summary

Nature Portfolio wishes to improve the reproducibility of the work that we publish. This form provides structure for consistency and transparency in reporting. For further information on Nature Portfolio policies, see our Editorial Policies and the Editorial Policy Checklist.

Statistics

For all statistical analyses, confirm that the following items are present in the figure legend, table legend, main text, or Methods section.

n/a	Confirmed
☐	☒ The exact sample size (*n*) for each experimental group/condition, given as a discrete number and unit of measurement
☐	☒ A statement on whether measurements were taken from distinct samples or whether the same sample was measured repeatedly
☐	☒ The statistical test(s) used AND whether they are one- or two-sided *Only common tests should be described solely by name; describe more complex techniques in the Methods section.*
☐	☒ A description of all covariates tested
☐	☒ A description of any assumptions or corrections, such as tests of normality and adjustment for multiple comparisons
☐	☒ A full description of the statistical parameters including central tendency (e.g. means) or other basic estimates (e.g. regression coefficient) AND variation (e.g. standard deviation) or associated estimates of uncertainty (e.g. confidence intervals)
☐	☒ For null hypothesis testing, the test statistic (e.g. *F*, *t*, *r*) with confidence intervals, effect sizes, degrees of freedom and *P* value noted *Give P values as exact values whenever suitable.*
☒	☐ For Bayesian analysis, information on the choice of priors and Markov chain Monte Carlo settings
☒	☐ For hierarchical and complex designs, identification of the appropriate level for tests and full reporting of outcomes
☐	☒ Estimates of effect sizes (e.g. Cohen's *d*, Pearson's *r*), indicating how they were calculated

Our web collection on statistics for biologists contains articles on many of the points above.

Software and code

Policy information about availability of computer code

Data collection	EPIC EHR software v2023 (retrospective EMR review and clinical data aggregation) and REDCap v13.7.31 (clinical data aggregation).
Data analysis	FlowJo (v10.10, Tree Star), GraphPad Prism (v10.0.0), Python (v3.8.16), scprep (v1.2.3), scanpy (v1.10), PhenoGraph (v1.5.1), R (v4.2.3), logistf (v1.26.0), gseapy (v1.1.8), survminer (v0.5.0), tidyverse (v2.0.0)

For manuscripts utilizing custom algorithms or software that are central to the research but not yet described in published literature, software must be made available to editors and reviewers. We strongly encourage code deposition in a community repository (e.g. GitHub). See the Nature Portfolio guidelines for submitting code & software for further information.

Data

Policy information about availability of data

All manuscripts must include a data availability statement. This statement should provide the following information, where applicable:

- Accession codes, unique identifiers, or web links for publicly available datasets
- A description of any restrictions on data availability
- For clinical datasets or third party data, please ensure that the statement adheres to our policy

All data used to generate figures and tables in this study are included in the Source Data. The scRNA-seq data generated from this study have been deposited in the Gene Expression Omnibus (GEO) under accession number GSE294482. The reference dataset used in extended data figure 8 is under GEO accession number

GSE199563. REAP data will be made available upon reasonable request, subject to restrictions related to patient privacy in accordance with institutional policies and the Health Insurance Portability and Accountability Act (HIPAA).

Research involving human participants, their data, or biological material

Policy information about studies with human participants or human data. See also policy information about sex, gender (identity/presentation), and sexual orientation and race, ethnicity and racism.

Reporting on sex and gender	Sex was determined through self-report and review of electronic medical records. No sex disaggregated analysis was performed. Study demographics, including proportion sex by individual study group, are included in Extended Table 1.
Reporting on race, ethnicity, or other socially relevant groupings	No race, ethnicity or other socially relevant groupings were used in this study.
Population characteristics	All relevant population demographics are described in Extended Table 1.
Recruitment	Yale cohort. Patients were approached at Yale New Haven Hospital upon initiating or while receiving treatment with anti-PD-1, anti-PD-L1, or anti-PD-1 combined with anti-CTLA-4. They were invited to participate by donating blood and clinical data. All patients with available samples and relevant clinical data were included for REAP processing, without any additional selection bias. MT cohort. The MT Group collected samples from multiple sources, including academic centers, community hospitals, and private practices. All patients receiving checkpoint inhibitors with available samples and relevant clinical data were included for REAP processing, without any additional selection bias.
Ethics oversight	For the Yale cohort, the study was conducted with approval from the Yale University Institutional Review Board (HIC# 0608001773, HIC# 1512016953, HIC# 1401013290), and written informed consent was obtained from all participants. For the MT cohort, approval was obtained from local IRBs and a central IRB (Sterling). All patient samples and clinical data elements were de-identified, and all protected health information was removed in accordance with the Health Insurance Portability and Accountability Act (HIPAA).

Note that full information on the approval of the study protocol must also be provided in the manuscript.

Field-specific reporting

Please select the one below that is the best fit for your research. If you are not sure, read the appropriate sections before making your selection.

☒ Life sciences ☐ Behavioural & social sciences ☐ Ecological, evolutionary & environmental sciences

For a reference copy of the document with all sections, see nature.com/documents/nr-reporting-summary-flat.pdf

Life sciences study design

All studies must disclose on these points even when the disclosure is negative.

Sample size	Sample size was not predetermined prior to enrollment of study participants. Samples sizes were chosen based on prior experience with REAP study, multiplexed immune phenotyping assays and available study resources.
Data exclusions	No data were excluded from the analyses.
Replication	All experiments not involving mice were performed with technical replicates. All mouse experiments were repeated at least twice, and the exact number of mice included in each group was indicated in the paper. All data presented in the figures were pooled from at least two independent experiments.
Randomization	Randomization was not applicable to REAP screening as it was a cross-sectional, observational human research study of a pre-existing medical condition. For autoantibody ELISA validations and functional assays, randomization was not applicable, as the experiments compared samples from predefined groups based on autoantibody positivity identified in our REAP screen. Controlling for other covariates was not necessary, as autoantibody positivity was the sole stratifying factor of interest. For mouse experiments, age- and sex-matched mice were randomly assigned to experimental groups at the start of the in vivo studies.
Blinding	For human samples, the process of (1) sample and clinical data collection, (2) REAP data generation and analysis, and (3) REAP-clinical data correlation was performed by separate scientists. Clinical information and patient groupings were only revealed after REAP data analysis was complete. A separate clinical team performed chart reviews and assigned clinical scores. For autoantibody ELISA validations, autoantibody functional assays and mouse experiments, investigators were not blinded as there was no subjective measurement.

Reporting for specific materials, systems and methods

We require information from authors about some types of materials, experimental systems and methods used in many studies. Here, indicate whether each material, system or method listed is relevant to your study. If you are not sure if a list item applies to your research, read the appropriate section before selecting a response.

Materials & experimental systems

n/a	Involved in the study
☐	☒ Antibodies
☐	☒ Eukaryotic cell lines
☒	☐ Palaeontology and archaeology
☐	☒ Animals and other organisms
☒	☐ Clinical data
☒	☐ Dual use research of concern
☒	☐ Plants

Methods

n/a	Involved in the study
☒	☐ ChIP-seq
☐	☒ Flow cytometry
☒	☐ MRI-based neuroimaging

Antibodies

Antibodies used

REAP assay:
Biotin anti-hIgG (HP6017), 1:100, 409308, BioLegend

ELISA:
HRP anti-hIgG (M1308A10), 1:5000, 410603, BioLegend
HRP anti-hIgG1 (HP6001), 1:5000, 9054-05, Southern Biotech
HRP anti-hIgG2 (31-7-4), 1:5000, 9060-05, Southern Biotech
HRP anti-hIgG3 (HP6050), 1:5000, 9210-05, Southern Biotech
HRP anti-hIgG4 (HP6025) 1:5000, 9200-05, Southern Biotech

Mouse tumor treatment study:
anti-mPD-1 (RP1-14), 200 µg/dosage, Bio X Cell
anti-mCTLA-4 (9H10), 100 µg/dosage, Bio X Cell
anti-mIFNAR-1 (MAR1-5A3), 1 mg/dosage, Bio X Cell
anti-mIFNA (TIF-3C5), 500 µg/dosage, Ichorbio
anti-mTL1A (5G4.6), 200 µg/dosage, Bio X Cell

Anti-human antibodies used in human PBMC immunophenotyping:
anti-hCD3 (UCHT1), 1:100, Pacblue, #300431, BioLegend
anti-hCD4 (OKT4), 1:200, FITC, #317408, BioLegend
anti-hCD8 (SK1), 1:400, cFluor V547, #SKU R7-20063, CYTEK
anti-hCD14 (63D3), 1:200, Spark Blue 550, #367148, BioLegend
anti-hCD16 (3G8), 1:200, BV570, #302036, BioLegend
anti-hCD19 (SJ25C1), 1:400, BUV496, #612938, BD Biosciences
anti-hCD56 (NCAM16.2), 1:800, BUV737, #564447, BD Biosciences
anti-hCD28 (CD28.2), 1:200, PE-Fire 810, #302971, BioLegend
anti-hCD45 (2D11), 1:200, PerCP, #67-9459-T100, Tonbo Biosciences
anti-hCD27 (O323), 1:200, BUV563, #751679, BD Biosciences
anti-hCD123 (6H6), 1:200, BB515, #567715, BD Biosciences
anti-hCD11c (3.9), 1:400, PerCP-Cy5.5, #301624, BioLegend
anti-hIgD (IA6-2), 1:200, PE-Cy7, #348210, BioLegend
anti-hIgM (MHM-88), 1:200, BV711, #314540, BioLegend
anti-hIgG (G18-145), 1:200, BV605, #563246, BD Biosciences
anti-hCXCR5 (RF8B2), 1:200, BUV805, #741980, BD Biosciences
anti-hCD141 (1A4), 1:200, BV421, #565321, BD Biosciences
anti-hCD1c (L161), 1:200, Alexa Fluor 647, #331510, BioLegend
anti-hLAIR-1(REA447), 1:10, APC, #130-106-806, Milteney Biotech
anti-hSiglec-1(7-239), 1:100, PE/Dazzle™ 594, #346016, BioLegend
anti-hCD163 (GHI/61), 1:200, APC/Cy 7, #333622, BioLegend
anti-hCD68 (Y1/82A), 1:200, R718, #568069, BD Biosciences

Anti-mouse antibodies used in mouse flow cytometry experiments:
anti-mCD45 (30-F11), 1:400, BUV496, #364-0451-82, eBioscience
anti-mCD3 (17A2), 1:400, BUV615, #751418, BD Biosciences
anti-mCD4 (GK1.5), 1:100, Spark Blue™ 550, #100474, BioLegend
anti-mCD4 (GK1.5), 1:400, PerCP, #100432, BioLegend
anti-mCD8a (53-6.7), 1:200, Alexa Fluor® 700, #100729, BioLegend
anti-mCD49b (DX5), 1:400, BV650, #740496, BD Biosciences
anti-mTL1A (Tandys1a), 1:400, PerCP-eFluor™ 710, #46-7911-82, eBiosceience
anti-mDR3 (4C12), 1:400, PE, #144405, BioLegend

anti-mPD-1 (RMP1-30), 1:200, BB515, #566832, BD Biosciences
anti-mTIM3 (RMT3-23), 1:800, BV711, #119727, BioLegend
anti-mIFNγ (XMG1.2), 1:200, violetFluor™ 450, #75-7311-U100, Tonbo Bioscience
anti-mIL-10 (JES5-16E3), 1:200, BV605, #505031, BioLegend
anti-mPerforin (S16009A), 1:400, FITC, #154310, BioLegend
anti-mTNFα (MP6-XT22), 1:800, PE/Dazzle™ 594, #506346, BioLegend
anti-mKi67 (16A8), 1:200, PE, #652404, BioLegend
anti-mGranzyme B (QA16A02), 1:200, PerCP-Cy5.5, #372212, BioLegend
anti-mCaspase3 (C92605), 1:5, FITC, #559341, BD Biosciences

Validation

The antibody validation is provided on suppliers' website (supplier information is included above). All antibodies were validated with proper isotype controls by flow cytometry.

Eukaryotic cell lines

Policy information about cell lines and Sex and Gender in Research

Cell line source(s)	TF-1 cell (ATCC, CRL-2003), THP-1 cell (ATCC, TIB-202), Expi293F cell (Thermo Fisher Scientific, A14527), MC38 (Yale, M. Bosenberg), CT-26 (ATCC, CRL-2638), B16-F10 (ATCC, CRL-6475)
Authentication	The TF-1 cell line, THP-1 cell line, and Expi293F cell line, CT-26 and B16-F10 were purchased commercially and not authenticated by us. MC38 was previously reported but not authenticated by us.
Mycoplasma contamination	No cell lines were tested for mycoplasma contamination.
Commonly misidentified lines (See ICLAC register)	none

Animals and other research organisms

Policy information about studies involving animals; ARRIVE guidelines recommended for reporting animal research, and Sex and Gender in Research

Laboratory animals	8–10 week-old C57BL/6 and BALB/c mice from purchased from Charles River Laboratories. Mice were housed in groups of 5 to 6 per cage and maintained under specific-pathogen-free conditions on a 12-hour light/dark cycle (lights on at 7:00 AM), at a temperature of 22–25°C and relative humidity of 30–70%. All mice had ad libitum access to regular rodent chow and sterilized water.
Wild animals	No wild animals were used.
Reporting on sex	Female C57BL/6 and BALB/c mice were used for tumor study.
Field-collected samples	No filed-collected samples were used.
Ethics oversight	All procedures used in this study complied with federal guidelines and the institutional policies of the Yale School of Medicine Animal Care and Use Committee.

Note that full information on the approval of the study protocol must also be provided in the manuscript.

Plants

Seed stocks	*Report on the source of all seed stocks or other plant material used. If applicable, state the seed stock centre and catalogue number. If plant specimens were collected from the field, describe the collection location, date and sampling procedures.*
Novel plant genotypes	*Describe the methods by which all novel plant genotypes were produced. This includes those generated by transgenic approaches, gene editing, chemical/radiation-based mutagenesis and hybridization. For transgenic lines, describe the transformation method, the number of independent lines analyzed and the generation upon which experiments were performed. For gene-edited lines, describe the editor used, the endogenous sequence targeted for editing, the targeting guide RNA sequence (if applicable) and how the editor was applied.*
Authentication	*Describe any authentication procedures for each seed stock used or novel genotype generated. Describe any experiments used to assess the effect of a mutation and, where applicable, how potential secondary effects (e.g. second site T-DNA insertions, mosiacism, off-target gene editing) were examined.*

Flow Cytometry

Plots

Confirm that:

☒ The axis labels state the marker and fluorochrome used (e.g. CD4-FITC).

☒ The axis scales are clearly visible. Include numbers along axes only for bottom left plot of group (a 'group' is an analysis of identical markers).

☒ All plots are contour plots with outliers or pseudocolor plots.

☒ A numerical value for number of cells or percentage (with statistics) is provided.

Methodology

Sample preparation	Human PBMC: Human frozen PBMCs from patients were thawed in RMPI+10% FBS medium in presence of Benzonase (Sigma-Aldrich, E8263-25KU) and washed with PBS buffer twice before staining. Mouse tumor sample: Digestion media (RPMI-1640 supplemented with 1% FBS, 1 mg/ml Collagenase IV (Thermo Fisher Scientific, 17104019) and 0.2 mg/ml Dnase I (Sigma-Aldrich, 10104159001)) was pre-warmed in 37 °C. Tumor tissues were minced and incubated in digestion media for 20 minutes at 37°C with shaking. Then, R10 media (RPMI-1640 with 10% FBS) was added to neutralize protease activity and tumor tissues were smashed through 70 µM cell strainers to prepare single-cell suspensions. Cells were then washed twice with R10 media. ACK buffer (Thermo Fisher Scientific, A1049201) was then used for red blood cell lysis, followed by two times wash with R10 media. In final, cells were resuspended in 1 ml R10 media for downstream staining. Cell concentration was counted by a CellDrop Automated Cell Counter (DeNovix).
Instrument	Cytek Aurora [Spectral Flow Cytometry] for analysis, BD FACSAriaII for sorting
Software	FlowJo (Version 10, Tree Star)
Cell population abundance	Post-sort purity was routinely >90% as determined by FACS.
Gating strategy	Gating strategies are available in supplementary figures. Flow cytometry gating for Figures 3c–d, 3h–i, and 4j–k has now been included in the Extended Data Figures: 3c–d in Extended Data Figure 5b, 3h–i in Extended Data Figure 5f, and 4j–k in Extended Data Figure 7f. The corresponding Extended Data Figure legends have also been updated.

☒ Tick this box to confirm that a figure exemplifying the gating strategy is provided in the Supplementary Information.